

N73-29393

The Influence of Ozone and Aerosols on the Brightness and Color
of the Twilight Zone

by

Charles N. Adams, Gilbert N. Plass, and George W. Kattawar

Report No. 7

The Research described in this report was

funded by the

National Aeronautics and Space Administration

Contract No. NGR 44-001-117

Department of Physics
Texas A & M University
College Station, Texas 77843

**CASE FILE
COPY**

July 15, 1973

A paper based on the material in this report has been submitted
to the Journal of Atmospheric Sciences.

The Influence of Ozone and Aerosols on the Brightness and Color
of the Twilight Sky

By Charles N. Adams, Gilbert N. Plass, and George W. Kattawar

Department of Physics, Texas A & M University, College Station, Texas 77843

ABSTRACT

The radiance and color of the twilight sky are calculated for single scattered radiation with the use of spherically symmetric models of the earth's atmosphere. Spherical geometry is used throughout the calculations with no plane parallel approximations. Refraction effects are taken into account through fine subdivision of the atmosphere into spherical shells of fixed index of refraction. Snell's law of refraction is used to calculate a new direction of travel each time that a photon traverses the interface between layers. Five different models of the atmosphere were used: a pure molecular scattering atmosphere; molecular atmosphere plus ozone absorption; three models with aerosol concentrations of 1, 3, and 10 times normal together with molecular scattering and ozone absorption. The results of the calculations are shown for various observation positions and local viewing angles in the solar plane for wavelengths in the range of 0.40μ to 0.75μ .

1. INTRODUCTION

Numerous difficult problems arise in the study of twilight in the earth's atmosphere whether by theoretical techniques or physical measurements. Each physical sunrise and sunset is unique, unrepeatable, and highly dynamic. The dynamic changes in intensities and spectral distributions (the observed color) as a function of viewing angle and relative position of the observer to the sun produce many problems in equipment construction and rapid data accumulation and analysis. Furthermore, the observer does not know what viewing angles may yield the most useful information at a given time.

The theoretical calculations for simple atmospheric models are repeatable, but may not reproduce all that is physically observed. This is to be expected. The relatively simple treatment of this article which assumed that the photons were scattered only once required an appreciable amount of computer time on the CDC 7600 high speed digital computer and produced a proportional amount of information to be processed. A later article by the authors will show how more suitable results may be obtained by the addition of multiple scattering effects.

Hulbert (1953) attempted to determine quantitatively the brightness and color of the twilight sky. He showed the importance of ozone in determining the blue color of the zenith twilight sky. Rozenberg (1963) has examined these problems in great detail in his book. Most of his discussion is essentially qualitative and is based on approximate equations whose validity is difficult to assess. All of his results are for a single scattering model with no refraction.

The most recent and comprehensive article on the subject is by Dave and Mateer (1968). They show colorimetry results for five atmospheric models

(similar to the ones used in this article), but do not include any refraction or multiple scattering effects. A similar treatment is used in the following calculations with the important difference that the refraction of the light rays is taken into account.

2. COMPUTATIONAL TECHNIQUES

The geometry of the problem for the solution of the observed radiance at a point P on the earth's surface is illustrated in Figure 1. The quantity y in the figure is the minimum height of the direct solar beam above the earth's surface if there were no refraction (while h_m is the same quantity when refraction is considered). The radius of the earth R_e is taken as 6371 km in the calculation.

The radiance I_λ of the single scattered radiation as received by the observer at point P on the earth's surface is given by the equation

$$I_\lambda(\theta_o, \theta) = \int_0^\infty (\beta_R P_R(\mu) + \beta_M P_M(\mu)) F_s(\lambda) T_p ds, \quad (1)$$

where

θ_o = solar zenith angle with respect to the vertical of the observer.

θ = local zenith viewing angle for the observer.

β_R = volume scattering coefficient for Rayleigh scattering.

$P_R(\mu)$ = Rayleigh phase function for scattering angle μ .

β_M = volume scattering coefficient for aerosol scattering.

$P_M(\mu)$ = aerosol phase function for scattering angle μ .

$F_s(\lambda)$ = incident solar flux upon scattering volume. This expression

may be written as the product of $F_0(\lambda)T_s$, where T_s is fractional transmission for direct solar beam to the scattering point and $F_0(\lambda)$ is the extraterrestrial solar flux at wavelength λ .

T_p = fractional transmission of scattered light from the scattering point to the observer.

The formulas for $F_s(\lambda)$ and T_p are given by

$$T_s = \exp(-\int_0^L (\beta_R(\lambda) + \beta_3(\lambda) - \beta_m(\lambda)) d\lambda), \quad (2)$$

and

$$T_p = \exp(-\int_0^S (\beta_R(s') + \beta_3(s') + \beta_m(s')) ds') \quad (3)$$

where

β_3 = volume absorption coefficient for ozone.

L = total distance traversed by photon from point of entrance into the model atmosphere to scattering point along the curved path.

S = total distance from observation point to scattering point along the line of sight.

The integral in (1) was evaluated by Simpson's rule from the single scattering contributions at the points of intersection of the solar rays with the line of sight from the observer. The integrals in (2) and (3) were reduced to sums of products of extinction coefficients and distances traversed through the atmospheric layers of the model.

3. COLORIMETRY

A system of coordinates called the tristimulus values provides a standard quantitative measurement of the color response of the human eye to a spectral distribution. The standard luminosity functions \bar{x}_λ , \bar{y}_λ , and \bar{z}_λ have been given in tabular form by many authors for intervals of 0.005μ .

The values used in these calculations are from the tables of Wyszecki and Stiles (1967).

The tristimulus values X, Y, and Z are obtained from the standard luminosity functions \bar{x}_λ , \bar{y}_λ , and \bar{z}_λ for a particular spectral distribution of radiant flux represented by $I_\lambda d\lambda$ from the equations

$$\begin{aligned} X &= \int I_\lambda \bar{x}_\lambda d\lambda, \\ Y &= \int I_\lambda \bar{y}_\lambda d\lambda, \\ Z &= \int I_\lambda \bar{z}_\lambda d\lambda. \end{aligned} \tag{4}$$

Finally the chromaticity coordinates x, y, and z are obtained from the expressions

$$\begin{aligned} x &= X (X + Y + Z)^{-1}, \\ y &= Y (X + Y + Z)^{-1}, \\ z &= Z (X + Y + Z)^{-1}, \end{aligned} \tag{5}$$

Since the sum of x, y, and z is unity, only two of the chromaticity coordinates need be specified.

The chromaticity coordinates for twilight were calculated from the radiance calculated from (1) and substituted in (4) and (5). The radiance was calculated for the wavelengths 0.40μ [0.05] 0.75μ . Since the radiance is a slowly varying function of wavelength, the calculated values were fitted by a cubic spline routine in order to obtain radiance values for any wavelength in this interval. These radiance values were weighted with the solar spectral irradiance distribution at the top of the atmosphere as given by Thekaekara (1972) and by the appropriate standard luminosity functions. Thus the integral in (4) was calculated and finally the chromaticity coordinates were obtained from (5).

4. ATMOSPHERIC MODELS

Five different atmospheric models were used for the calculations which are referred to as models A, B, C, D, and E. These models have the following characteristics: A, pure molecular scattering; B, molecular scattering plus ozone absorption; C, molecular scattering, ozone absorption, and normal aerosol concentration as tabulated by Elterman (1968); D, as model C, but with three times normal aerosol concentration; E, as model C, but with ten times normal aerosol concentration.

The model atmosphere is assumed to have concentric spherical shells of thickness 1 km from the radius of the earth, R_e , to $R_e + 400$ km and shells of thickness 5 km from an altitude of 400 km to 500 km. Atmospheric parameters are taken as constant in each layer. The density values are obtained from the U. S. Standard Atmosphere 1962, Anonymous (1965). Atmospheric extinction coefficients for Rayleigh, ozone, and aerosol scattering are obtained from the tables of Elterman (1968) for altitudes up to 50 km. Above this altitude Rayleigh extinction coefficients are calculated from density values obtained from the U. S. Standard Atmosphere 1962, ozone extinction coefficients are assumed to be zero, and aerosol extinction coefficients are assumed to decrease from 50 to 80 km with the same scale height as from 40 to 50 km. The number density of the aerosols is held constant from 80 to 90 km in order to simulate an aerosol layer. Above 90 km the aerosol number density decreases with the same scale height already used. The calculated optical thickness of the entire atmosphere in the zenith direction as a function of wavelength is shown in Fig. 2 for each of the five models.

The shadow height for a given line of sight of the observer is defined as the vertical height to the point along the line of sight that intersects

the path of a solar photon that just grazes the earth's surface. The shadow height is shown in Fig. 3 as a function of the zenith angle θ of the line of sight taken as positive in the solar direction and negative in the antisolar direction. Each curve is for a particular value of θ_0 which defines the observer's position on the earth's surface with respect to the solar direction (see Fig. 1). The solid curves give the shadow height when refraction effects are taken into account and the dashed curves are calculated without refraction. The dashed curves agree well with the results of Rosenberg (1963). In many cases there is an important change in the shadow height when refraction is taken into account. These decreased shadow heights increase the radiance contributions from lower altitudes, particularly at longer wavelengths where the atmosphere is more transparent. This in turn changes the calculated colorimetry values.

As another example of the importance of refraction, particularly for the rays that come close to the earth's surface, consider an observer at the terminator ($\theta_0 = 90^\circ$) viewing an unrefracted solar ray at the zenith ($\theta = 0^\circ$) that intersects the line of sight at an altitude of 2 km. The refracted ray intersects the line of sight instead at 0.55 km. When looking in the antisolar direction so that $\theta = -85^\circ$, the same unrefracted and refracted rays intersect the line of sight at 2.04 km and 0.51 km respectively.

The transmission from outside the atmosphere to the perigee point is shown in Figs. 4 and 5 for $\lambda = 0.45\mu$ and 0.75μ respectively. The transmission for Model A is much greater at $\lambda = 0.75\mu$ than at 0.45μ because of the strong wavelength dependence of Rayleigh scattering. The ozone absorption is small at $\lambda = 0.45\mu$ and the difference between the curves for Models A and B cannot be shown on the scale of the figure. The transmission is always less at a shorter wavelength than at a longer when a given model and perigee height

are compared. The greatest changes between these figures occur in those regions of Fig. 5 with relatively high transmission and a perigee height near the earth's surface.

5. CALCULATED RADIANCE

The single scattered radiance was calculated for the following observer positions: $\theta_o = 80^\circ, 85^\circ, 90^\circ [2^\circ] 108^\circ$. At each observer position calculations were made for the following zenith viewing angles in the solar plane: $\theta = 90^\circ, 85^\circ, 80^\circ, 75^\circ, 70^\circ [10^\circ] -70^\circ, -75^\circ, -80^\circ, -85^\circ$, where positive values of θ refer to viewing angles in the solar direction from the zenith while negative values are in the antisolar direction. All calculations were performed for 8 wavelengths: $0.40\mu [0.05] 0.75\mu$.

The radiance calculated for Model A is shown in Figs. 6 and 7 as a function of wavelength for $\theta_o = 90^\circ$ and various viewing angles θ . All calculated radiance values assume an incident solar flux of unity perpendicular to the incoming solar beam at each wavelength. Later these values are weighted by the solar distribution for the calculation of the colorimetry results. In the solar direction, Figure 6 shows that the greatest change with wavelength occurs when $\theta = 85^\circ$, the large decrease in the blue caused by the increased Rayleigh scattering at shorter wavelengths. As the viewing angle increases from 85° to the zenith, the radiance in the blue increases at first and then decreases. There are three competing effects as θ decreases: first, an increase due to less absorption of solar radiation along the ray to the scattering center; second, the number of scattering centers along the line of sight decreases by the secant effect; third, the absorption decreases from the scattering center to the observer. The radiance in the antisolar directions is shown in Fig. 7.

The radiance in the solar directions for Model B is given in Fig. 8 for $\theta_o = 90^\circ$. The radiance for a fixed value of θ now shows a pronounced minimum near $\lambda = 0.6\mu$ due to the ozone absorption.

The radiance for Model C when $\theta_o = 90^\circ$ is given in Fig. 9 for viewing angles in the solar direction. Rayleigh scattering, ozone absorption, and aerosol scattering are all included in this model. The dip in the radiance curves in the middle of the visible spectrum due to ozone absorption is clearly visible here. In most cases the radiance is less for Model C than for Model A except at long wavelengths and for viewing angles near the horizon. In this case the radiance is larger due to the strong forward scattering of the sunlight by the aerosols and the additional scattering centers along the line of sight.

A more complete understanding of these curves can be obtained by a study of the differential radiance curves shown in Fig. 10. The differential radiance per kilometer (measured along the slant path) is given as a function of the vertical height to the scattering volume measured along the earth's local radius through the infinitesimal volume. Each curve for a particular value of θ increases to a maximum value; beyond the maximum it decreases approximately as an exponential. The initial increase in the radiance occurs as the transmission of the solar radiation to the scattering point increases with height. The differential radiance eventually decreases as the number of scattering centers of all types decreases with height. At altitudes above 60 km these curves are identical on the scale of this figure for the same zenith angle in the solar and antisolar directions (e.g. $\theta = 70^\circ$ and $\theta = -70^\circ$). The curves for an observer at the terminator have this symmetry at altitudes sufficiently high that there is virtually no loss in the solar radiation to the scattering

point on either line of sight. At lower altitudes the differential radiance is lower in the antisolar direction because of the additional absorption of the solar beam before it reaches the scattering point (e.g., the curve for $\theta = -85^\circ$ is considerably lower below an altitude of 40 km than that for $\theta = 85^\circ$). Since the radiance observed at a given angle of view is proportional to the area under the corresponding differential radiance curve in Fig. 10, the variation in the radiance curves with θ can be understood in terms of the changes in the absorption of the solar beam up to the point of scattering, the dependence of the scattering on the phase function of the aerosols and the Rayleigh scattering centers, the decrease of the scattering centers with height, and the secant variation of the number of scattering centers along the line of sight.

The radiance for Model B and $\theta_0 = 96^\circ$ is shown in Fig. 11. The radiance for Model C and $\theta_0 = 96^\circ$ is given in Figs. 12 and 13 for the solar and antisolar directions respectively. In general the difference in radiance between Models B and C is greater at long wavelengths than at short. This is largely due to the much greater difference between Models B and C in the transmission through the atmosphere up to the scattering point at longer wavelengths (Fig. 5) than at shorter (Fig. 4). The radiance in the antisolar direction shows little dependence on θ until $\theta = -40^\circ$. The radiance rapidly decreases to very small values for larger zenith angles.

The differential radiance for $\theta_0 = 96^\circ$ is given in Fig. 14. The differential radiance at the zenith reaches a maximum at about 62 km. The maxima for $\theta = 40^\circ$ and $\theta = -40^\circ$ occur approximately at 57 and 67 km respectively. The curves for $\theta = 0^\circ$, 40° , and -40° are nearly the same on

the scale of the figure above 75 km. Below 90 km the differential radiance for $\theta = -70^\circ$ is very much less than that for $\theta = 70^\circ$ due to the much greater atmospheric path that the solar rays must traverse to reach the scattering point in the former case. The maxima for these two angles are at about 50 and 82 km respectively. The maximum for $\theta = 85^\circ$ is at about 35 km. No single scattered radiation can be observed at $\theta = -85^\circ$ up to the altitudes considered here.

6. CHROMATICITY

The chromaticity was calculated for each model and solar zenith angle by the method described in Section 3. The results are shown in a series of chromaticity diagrams in which the x and y chromaticity coordinates are plotted for each viewing angle in the solar and antisolar half planes. For further reference the chromaticity coordinates are given in Tables 1 to 4 for each of the five models, for various values of θ , and for $\theta_o = 90^\circ$, 92° , 94° , and 96° .

Model A. Molecular atmosphere without ozone. The chromaticity diagrams for Model A are shown in Figs. 15 and 16 for $\theta_o = 90^\circ$, 92° , and 96° . The regions traditionally assigned to the different colors are indicated in Fig. 15 for guidance. The spectral purity isopleths are indicated in all the figures. When the spectral purity is less than about 5% the color is usually assumed to be a white or gray without discernable color. The numbers beside the curve indicate the zenith angle of observation (positive for the solar half plane and negative for the antisolar half plane). The colors for $\theta_o = 90^\circ$ are all yellow or an essentially white color near the zenith. At $\theta_o = 92^\circ$ and 96° the colors near the horizon have slightly greater spectral purity. A portion of these latter curves is also in the orange portion of the spectrum. The zenith sky is not blue in this model. The

actual colors of the twilight sky are not well represented by this model, except for the predominantly yellow-orange color just above the solar horizon.

For comparison, results were obtained in some cases both with and without consideration of the effects of refraction in the atmosphere. For example, at $\theta_o = 96^\circ$ and $\theta = 0^\circ$, $x = 0.351$ and $y = 0.346$ when refractive effects are taken into account, but $x = 0.316$ and $y = 0.327$ without refraction. In all cases calculated the x and y values were less without refraction than the same values obtained with refraction. Thus values calculated without refraction tend to be too far down on the chromaticity diagram and in many cases would show blue or purple colors that do not exist when refraction effects are included. This may explain some of the differences between our results and those of Dave and Mateer (1968). Other differences include the use of somewhat different atmospheric models and the extension of the atmosphere to much higher altitudes (500 km) in the present calculations.

Model B. Molecular atmosphere with ozone. The results when 0.35 cm of ozone are added to the molecular atmosphere are shown in Figs. 17 and 18. The main change brought about by the addition of the ozone to the model is the development of blue color over a large area of the sky surrounding the zenith. This results from the ozone absorption by the Chappius bands in the vicinity of $\lambda = 0.6\mu$. The spectral purity of the zenith increases as θ_o increases from 92° to 96° . A portion of the sky is purple of a low spectral purity in the antisolar half plane in some of these cases. The chromaticity coordinates vary hardly at all near the zenith as θ changes. The actual turning point of the chromaticity curve occurs in the range from $\theta = 20$ to 30° for $\theta_o = 94^\circ$ and 96° . The turning point on the figures

has usually been marked 0° , since the chromaticity is the same at $\theta = 0^\circ$ and 30° on these figures.

The blue color of the zenith sky as well as a region of purple sky in the antisolar half plane are features which are obtained from this model which can not be explained by a purely Rayleigh scattering atmosphere.

Model C. Molecular atmosphere, ozone, normal aerosol amount. The results for this model of the normal atmosphere are shown in Figs. 19 and 20. The blue region of the sky around the zenith has a higher spectral purity when aerosols are added to the model. Dave and Mateer (1968) have pointed out that a normal aerosol amount contributes to an increased blueness of the zenith sky. The spectral purity is somewhat higher in our calculations than in theirs and becomes almost 40% near the zenith when $\theta_o = 96^\circ$. The greater increase in absorption at blue than at red wavelengths for the solar radiation up to the scattering point when Models B and C are compared (Figs. 4 and 5) is the reason for the deeper blue color at the zenith when aerosols are present. Some purple light of low spectral purity is predicted for some angles of observation.

The color of the sky around the solar horizon is correctly predicted as an orange-red of high spectral purity. The single scattering model predicts orange colors near the antisolar horizon as θ_o increases in disagreement with observation. Obviously multiple scattering effects are most important in this region of the sky. The chromaticity curve for $\theta_o = 94^\circ$ is not shown here since it is very nearly the same as for $\theta_o = 96^\circ$. The main difference is that the point $\theta = 80^\circ$ corresponds to a yellow-orange of spectral purity 18% when $\theta_o = 94^\circ$, but corresponds to a nearly white color when $\theta_o = 96^\circ$.

Model D. Molecular atmosphere, ozone, three times normal aerosol amount. The chromaticity diagram when the atmosphere contains three times the normal aerosol amount at all altitudes is shown in Fig. 21. At $\theta_0 = 92^\circ$ the portion of the sky near the solar horizon has a higher spectral purity and tends to appear a deeper red with the greater aerosol amount. The additional aerosols also make the sky around the zenith a blue of greater spectral purity and this color extends over a larger region of the sky. The more vivid colors which are observed at twilight during periods of high aerosol concentration in the atmosphere are confirmed by this model.

Model E. Molecular atmosphere, ozone, ten times normal aerosol amount. The chromaticity diagram when the atmosphere contains ten times the normal aerosol amount at all altitudes is shown in Fig. 22. This model represents an extreme condition with the optical thickness of the atmosphere in a vertical direction between 2 and 3.5 (Fig. 2). The region of the sky around the solar horizon with red and orange colors of high spectral purity continues to expand as the aerosol concentration increases up to this amount. For example, at $\theta_0 = 92^\circ$ the spectral purity is greater than 20% from the solar horizon to $\theta \sim 55^\circ$ for Model E; the corresponding values of θ for Models C and D are 78° and 76° . Furthermore the deep blue sky near the zenith has disappeared in Model E which has only a gray blue region within 30° of the zenith. These same features are also evident at $\theta_0 = 96^\circ$, although there is a larger region of blue sky around the zenith than at $\theta_0 = 92^\circ$. For large aerosol amounts the model indicates vivid colors near the solar horizon, but colors of reduced spectral purity near the zenith. Multiple scattering effects would be especially important for the larger optical depths of this model.

7. CONCLUSIONS

Molecular scattering alone cannot explain the colors of the twilight sky. The addition of ozone absorption is essential to a model in order to reproduce the blue of the zenith sky. Some purple colors of low spectral purity are also obtained from this model. The deep blue of the zenith sky and the red and orange colors of high spectral purity in the region of the sky around the solar horizon are obtained only when a realistic model is used which combines molecular, ozone, and aerosol scattering and absorption. When the aerosol amount is three times normal the blue of the zenith sky becomes deeper and extends over a greater area. However, when the aerosol amount is ten times normal the spectral purity of the blue of the zenith sky decreases appreciably. Larger regions of red and yellow colors of higher spectral purity around the solar horizon are predicted when the aerosol amount is greater than normal.

Refraction effects have been included in the present calculations. The greatest limitation of the present results is that they include only single scattering effects. We plan to use a Monte Carlo technique to extend these results to include all orders of multiple scattering.

This work was supported in part by grant NGR 44-001-117 from the National Aeronautics and Space Administration. Acknowledgement is made to the National Center for Atmospheric Research, which is sponsored by the National Science Foundation, for computer time used in this research.

REFERENCES

1. Anonymous, 1965: Handbook of Geophysics and Space Environments, United States Air Force, 653 pp.
2. Dave, J. V., and C. L. Mateer, 1968: The effect of stratospheric dust on the color of the twilight sky. *J. Geophy. Res.* 73, 6897-6913.
3. Elterman. L., 1968: UV, Visible, and IR Attenuation for Altitudes to 50 km, 1968, AFCRL-68-0153, United States Air Force, 49 pp.
4. Hulbert, E. O., 1953: Explanation of the brightness and color of the sky, particularly the twilight sky. *J. Opt. Soc. Amer.* 43, 113-118.
5. Rozenberg, G. V., 1963: Twilight: A Study in Atmospheric Optics, State Press for Physicomathematical Literature, Moscow; translated by R. G. Rodman, Plenum Press, New York, 358 pp.
6. Thekaekara, M. P., 1972: Evaluating the light from the sun. *Opt. Spectra* 5, 32-35.
7. Wyszecki, G., and W. S. Stiles, 1967: Color Science: Concepts and Methods, J. Wiley, New York, 628 pp.

TABLE I. COLORIMETRY VALUES FOR MODEL A

Θ_o	Θ	X	Y	Θ_o	Θ	X	Y
90	90	—	—	94	90	0.5597	0.4150
90	85	0.4048	0.4202	94	85	0.4274	0.4171
90	80	0.3633	0.3870	94	80	0.3831	0.3859
90	75	0.3465	0.3704	94	75	0.3672	0.3709
90	70	0.3379	0.3611	94	70	0.3601	0.3630
90	65	0.3328	0.3554	94	65	0.3563	0.3585
90	60	0.3294	0.3516	94	60	0.3541	0.3556
90	40	0.3234	0.3444	94	40	0.3516	0.3511
90	20	0.3217	0.3422	94	20	0.3525	0.3506
90	10	0.3216	0.3420	94	10	0.3525	0.3510
90	0	0.3213	0.3421	94	0	0.3549	0.3513
90	-10	0.3224	0.3428	94	-10	0.3563	0.3530
90	-20	0.3235	0.3439	94	-20	0.3595	0.3549
90	-40	0.3275	0.3493	94	-40	0.3692	0.3608
90	-60	0.3382	0.3595	94	-60	0.3899	0.3746
90	-65	0.3437	0.3650	94	-65	0.4014	0.3811
90	-70	0.3521	0.3730	94	-70	0.4194	0.3900
90	-75	0.3659	0.3855	94	-75	0.4612	0.4148
90	-80	0.3926	0.4065	94	-80	0.4963	0.3859
90	-85	0.4578	0.4395	94	-85	0.2249	0.0663
92	90	0.5596	0.4232	96	90	0.5723	0.4130
92	85	0.4261	0.4207	96	85	0.4619	0.4740
92	80	0.3823	0.3899	96	80	0.4342	0.4775
92	75	0.3655	0.3746	96	75	0.4235	0.4740
92	70	0.3572	0.3663	96	70	0.4174	0.4689
92	65	0.3525	0.3612	96	65	0.4125	0.4627
92	60	0.3495	0.3578	96	60	0.3302	0.3189
92	40	0.3446	0.3519	96	40	0.4224	0.4789
92	20	0.3438	0.3505	96	20	0.1846	0.0624
92	10	0.3441	0.3505	96	10	0.1919	0.0747
92	0	0.3448	0.3509	96	0	0.2023	0.0621
92	-10	0.3459	0.3518	96	-10	0.2153	0.1151
92	-20	0.3476	0.3532	96	-20	0.3572	0.3505
92	-40	0.3537	0.3582	96	-40	0.3697	0.3592
92	-60	0.3690	0.3704	96	-60	0.4041	0.3806
92	-65	0.3769	0.3763	96	-65	0.4250	0.3913
92	-70	0.3889	0.3846	96	-70	0.4617	0.4054
92	-75	0.4093	0.3970	96	-75	0.5298	0.4151
92	-80	0.4503	0.4153	96	-80	0.6061	0.3881
92	-85	0.5517	0.4184	96	-85	—	—

TABLE II. COLORIMETRY VALUES FOR MODEL B

Θ_0	Θ	X	Y	Θ_0	Θ	X	Y
90	90	—	—	94	90	0.5637	0.4124
90	85	0.3630	0.3907	94	85	0.3629	0.3652
90	80	0.3164	0.3448	94	80	0.3081	0.3125
90	75	0.2929	0.3238	94	75	0.2906	0.2910
90	70	0.2901	0.3125	94	70	0.2830	0.2804
90	65	0.2850	0.3056	94	65	0.2700	0.2743
90	60	0.2817	0.3011	94	60	0.2767	0.2705
90	40	0.2757	0.2925	94	40	0.2738	0.2642
90	20	0.2739	0.2897	94	20	0.2740	0.2629
90	10	0.2737	0.2893	94	10	0.2747	0.2629
90	0	0.2737	0.2893	94	0	0.2757	0.2635
90	-10	0.2742	0.2897	94	-10	0.2772	0.2645
90	-20	0.2749	0.2907	94	-20	0.2793	0.2661
90	-40	0.2783	0.2950	94	-40	0.2866	0.2720
90	-60	0.2877	0.3066	94	-60	0.3056	0.2874
90	-65	0.2927	0.3126	94	-55	0.3182	0.2955
90	-70	0.3004	0.3215	94	-70	0.3378	0.3080
90	-75	0.3137	0.3359	94	-75	0.3778	0.3297
90	-80	0.3415	0.3626	94	-90	0.4821	0.3638
90	-85	0.4203	0.4161	94	-95	0.6390	0.3555
92	90	0.5515	0.4228	96	90	0.5666	0.4069
92	85	0.3764	0.3843	96	95	0.3377	0.3464
92	80	0.3237	0.3359	96	90	0.2849	0.2935
92	75	0.3052	0.3145	96	75	0.2694	0.2731
92	70	0.2964	0.3033	96	70	0.2629	0.2631
92	65	0.2914	0.2957	96	65	0.2596	0.2574
92	60	0.2882	0.2922	96	60	0.2579	0.2538
92	40	0.2831	0.2844	96	40	0.2557	0.2477
92	20	0.2820	0.2821	96	20	0.2564	0.2466
92	10	0.2821	0.2819	96	10	0.2574	0.2468
92	0	0.2826	0.2820	96	0	0.2537	0.2476
92	-10	0.2835	0.2827	96	-10	0.2605	0.2489
92	-20	0.2849	0.2840	96	-20	0.2630	0.2509
92	-40	0.2902	0.2890	96	-40	0.2722	0.2595
92	-60	0.3046	0.3022	96	-60	0.3035	0.2829
92	-65	0.3125	0.3090	96	-65	0.3267	0.2994
92	-70	0.3250	0.3193	96	-70	0.3754	0.3299
92	-75	0.3478	0.3261	96	-75	0.4873	0.3784
92	-80	0.3997	0.3667	96	-80	0.6163	0.3717
92	-85	0.5471	0.4014	96	-85	—	—

TABLE III. COLORIMETRY VALUES FOR MODEL C

Θ_0	Θ	X	Y	Θ_0	Θ	X	Y
90	90	—	—	94	90	0.6731	0.3251
90	85	0.4672	0.4107	94	95	0.4582	0.3931
90	80	0.3912	0.3795	94	80	0.3745	0.3489
90	75	0.3583	0.3566	94	75	0.3366	0.3201
90	70	0.3403	0.3416	94	70	0.3152	0.3021
90	65	0.3289	0.3327	94	65	0.3007	0.2901
90	60	0.3211	0.3272	94	60	0.2897	0.2807
90	40	0.3000	0.3112	94	40	0.2608	0.2555
90	20	0.2852	0.2981	94	20	0.2467	0.2428
90	10	0.2709	0.2928	94	10	0.2416	0.2375
90	0	0.2731	0.2929	94	0	0.2376	0.2324
90	-10	0.2695	0.2794	94	-10	0.2352	0.2317
90	-20	0.2666	0.2755	94	-20	0.2340	0.2311
90	-40	0.2671	0.2792	94	-40	0.2355	0.2345
90	-60	0.2784	0.2940	94	-60	0.2456	0.2473
90	-65	0.2857	0.3022	94	-65	0.2519	0.2542
90	-70	0.2969	0.3142	94	-70	0.2427	0.2648
90	-75	0.3156	0.3324	94	-75	0.2859	0.2834
90	-80	0.3534	0.3629	94	-80	0.3748	0.3328
90	-85	0.4607	0.4119	94	-85	0.6607	0.3363
92	90	0.6695	0.3238	96	90	0.6778	0.3204
92	85	0.4609	0.4042	96	85	0.4304	0.3799
92	80	0.3854	0.3680	96	80	0.3250	0.3221
92	75	0.2517	0.2440	96	75	0.2931	0.2870
92	70	0.3334	0.2286	96	70	0.2626	0.2671
92	65	0.3218	0.3194	96	65	0.2509	0.2549
92	60	0.3122	0.3127	96	60	0.2433	0.2463
92	40	0.2884	0.2914	96	40	0.2291	0.2294
92	20	0.2727	0.2767	96	20	0.2244	0.2232
92	10	0.2663	0.2693	96	10	0.2231	0.2216
92	0	0.2599	0.2602	96	0	0.2224	0.2207
92	-10	0.2561	0.2567	96	-10	0.2222	0.2206
92	-20	0.2535	0.2539	96	-20	0.2224	0.2211
92	-40	0.2542	0.2556	96	-40	0.2248	0.2249
92	-60	0.2663	0.2710	96	-60	0.2354	0.2394
92	-65	0.2742	0.2791	96	-65	0.2472	0.2508
92	-70	0.2866	0.2908	96	-70	0.2774	0.2777
92	-75	0.3095	0.3098	96	-75	0.3909	0.3469
92	-80	0.3634	0.3437	96	-80	0.5826	0.3502
92	-85	0.5575	0.3944	96	-85	—	—

TABLE IV. COLORIMETRY VALUES FOR MODEL D

Θ_0	Θ	X	Y	Θ_0	Θ	X	Y
90	90	—	—	94	90	0.7124	0.2970
90	85	0.5294	0.4068	94	85	0.5144	0.4000
90	90	0.4305	0.3954	94	80	0.3969	0.3725
90	75	0.3841	0.3726	94	75	0.3429	0.3400
90	70	0.3592	0.3554	94	70	0.3140	0.3178
90	65	0.3440	0.3449	94	65	0.2950	0.3020
90	60	0.3343	0.3388	94	60	0.2932	0.2917
90	40	0.3113	0.3232	94	40	0.2532	0.2617
90	20	0.2955	0.3098	94	20	0.2401	0.2469
90	10	0.2892	0.3035	94	10	0.2355	0.2404
90	0	0.2795	0.2872	94	0	0.2222	0.2358
90	-10	0.2741	0.2816	94	-10	0.2304	0.2340
90	-20	0.2637	0.2752	94	-20	0.2296	0.2334
90	-40	0.2676	0.2770	94	-40	0.2316	0.2381
90	-50	0.2825	0.2967	94	-60	0.2414	0.2540
90	-65	0.2929	0.3076	94	-65	0.2470	0.2622
90	-70	0.3087	0.3233	94	-70	0.2555	0.2740
90	-75	0.3344	0.3450	94	-75	0.2701	0.2921
90	-80	0.3841	0.3760	94	-80	0.3114	0.3259
90	-85	0.5178	0.3995	94	-85	0.6991	0.3081
92	90	0.7118	0.2877	96	90	0.7126	0.2868
92	85	0.5256	0.4031	96	85	0.5011	0.3995
92	80	0.4195	0.3846	96	80	0.3676	0.3622
92	75	0.3685	0.3579	96	75	0.3082	0.3208
92	70	0.3416	0.3395	96	70	0.2787	0.2940
92	65	0.3251	0.3269	96	65	0.2620	0.2766
92	60	0.3140	0.3189	96	60	0.2516	0.2645
92	40	0.2860	0.2960	96	40	0.2331	0.2404
92	20	0.2690	0.2800	96	20	0.2270	0.2315
92	10	0.2615	0.2705	96	10	0.2254	0.2291
92	0	0.2535	0.2577	96	0	0.2245	0.2278
92	-10	0.2487	0.2529	96	-10	0.2240	0.2274
92	-20	0.2449	0.2494	96	-20	0.2241	0.2279
92	-40	0.2447	0.2513	96	-40	0.2240	0.2318
92	-60	0.2566	0.2685	96	-60	0.2332	0.2446
92	-65	0.2647	0.2785	96	-65	0.2382	0.2521
92	-70	0.2767	0.2920	96	-70	0.2497	0.2665
92	-75	0.2971	0.3126	96	-75	0.2889	0.3009
92	-80	0.3396	0.3447	96	-80	0.3206	0.3426
92	-85	0.5355	0.3702	96	-85	—	—

TABLE V. COLORIMETRY VALUES FOR MODEL E

Θ_o	Θ	X	Y	Θ_o	Θ	X	Y
90	85	0.6577	0.3379	94	85	0.6582	0.3367
90	80	0.5575	0.3963	94	80	0.5526	0.3936
90	75	0.4897	0.4046	94	75	0.4755	0.3988
90	70	0.4451	0.3963	94	70	0.4253	0.3873
90	65	0.4160	0.3872	94	65	0.3913	0.3744
90	60	0.3965	0.3800	94	60	0.3672	0.3523
90	40	0.3564	0.3615	94	40	0.3110	0.3240
90	30	0.3437	0.3529	94	30	0.2957	0.3099
90	20	0.3366	0.3495	94	20	0.2855	0.3016
90	10	0.3302	0.3445	94	10	0.2765	0.2912
90	0	0.3199	0.3270	94	0	0.2701	0.2836
90	-10	0.3151	0.3223	94	-10	0.2669	0.2809
90	-20	0.3096	0.3157	94	-20	0.2661	0.2807
90	-40	0.3135	0.3228	94	-40	0.2739	0.2921
90	-50	0.3247	0.3373	94	-50	0.2844	0.3048
90	-60	0.3482	0.3556	94	-60	0.3047	0.3258
90	-65	0.3706	0.3705	94	-65	0.3223	0.3418
90	-70	0.4033	0.3879	94	-70	0.3493	0.3626
90	-75	0.4517	0.4036	94	-75	0.3949	0.3876
90	-80	0.5283	0.4037	94	-80	0.4866	0.4008
90	-85	0.6485	0.3439	94	-85	0.6622	0.3295
92	85	0.6580	0.3373	96	85	0.6575	0.3372
92	80	0.5567	0.3935	96	80	0.5407	0.3974
92	75	0.4837	0.4009	96	75	0.4504	0.3975
92	70	0.4375	0.3914	96	70	0.3897	0.3777
92	65	0.4069	0.3815	96	65	0.3501	0.3563
92	60	0.3862	0.3730	96	60	0.3238	0.3380
92	40	0.3408	0.3485	96	40	0.2760	0.2946
92	20	0.3184	0.3332	96	20	0.2611	0.2777
92	10	0.3091	0.3232	96	10	0.2576	0.2733
92	0	0.2987	0.3078	96	0	0.2560	0.2714
92	-10	0.2931	0.3027	96	-10	0.2559	0.2715
92	-20	0.2884	0.2977	96	-20	0.2572	0.2735
92	-40	0.2932	0.3057	96	-40	0.2662	0.2853
92	-60	0.3267	0.3400	96	-60	0.2960	0.3181
92	-65	0.3476	0.3561	96	-65	0.3137	0.3341
92	-70	0.3777	0.3748	96	-70	0.3433	0.3562
92	-75	0.4249	0.3955	96	-75	0.3963	0.3873
92	-80	0.5029	0.4050	96	-80	0.4852	0.4135
92	-85	0.6445	0.3445	96	-85	—	—

Legends for Figures

Fig. 1. Geometry of direct solar flux to scattering point on line of sight and then to observer on the surface of the earth.

Fig. 2. Optical thickness through the entire atmosphere in a vertical direction as a function of wavelength for Models A (molecular absorption), B (ozone added), C (normal aerosol amount added), D (three times normal aerosol amount added), and E (ten times normal aerosol amount added).

Fig. 3. Shadow height in km as a function of θ , the zenith angle of observation. The solar horizon is at the right and the antisolar horizon at the left.

The angles marked on the curves are θ_o as defined in Fig. 1. The dashed curves are calculated without refraction, while the solid curves include the effect of the refraction of the light rays by the earth's atmosphere.

Fig. 4. The transmission of the solar radiation to the zenith direction as seen at the terminator as a function of perigee height of the solar ray.

Curves are shown for Models A, C, D, and E (the curve for Model B is the same as that for Model A on the scale of the figure) and for $\lambda = 0.45\mu$.

Fig. 5. Same as Fig. 4 except $\lambda = 0.75\mu$.

Fig. 6. Radiance as a function of wavelength (microns) for Model A and $\theta_o = 90^\circ$. The zenith angle of the direction of observation in the solar half plane is marked on each curve.

Fig. 7. Radiance as a function of wavelength (microns) for Model A and $\theta_o = 90^\circ$. The zenith angle of the direction of observation in the antisolar half plane is marked on each curve.

Fig. 8. Radiance for Model B and $\theta_o = 90^\circ$.

Fig. 9. Radiance for Model C and $\theta_o = 90^\circ$.

Fig. 10. The differential radiance per kilometer (measured along the slant path) as a function of the vertical height to the scattering volume measured along the earth's local radius through the infinitesimal volume. The results are for Model C, $\theta_o = 90^\circ$, and $\lambda = 0.4\mu$. Results are shown for $\theta = 85^\circ$, 70° , 40° , 0° , -40° , -70° , -85° (negative values are in the antisolar half plane).

Fig. 11. Radiance for Model B and $\theta_o = 96^\circ$.

Fig. 12. Radiance for Model C and $\theta_o = 96^\circ$ for solar half plane.

Fig. 13. Radiance for Model C and $\theta_o = 96^\circ$ for antisolar half plane.

Fig. 14. Differential radiance for Model C, $\theta_o = 96^\circ$, and $\lambda = 0.4\mu$.

See caption to Fig. 10.

Fig. 15. Chromaticity diagram for Model A and $\theta_o = 90^\circ$. The numbers on the curve indicate the value of θ (positive in the solar half plane and negative in the antisolar half plane). The spectral purity in percent is marked on the isopleths. The coordinates x and y are the chromaticity coordinates (see (5)). The generally accepted regions for the various colors are indicated on the diagram.

Fig. 16. Chromaticity diagram for Model A and $\theta_o = 92^\circ$ and 96° .

Fig. 17. Chromaticity diagram for Model B and $\theta_o = 90^\circ$ and 92° .

Fig. 18. Chromaticity diagram for Model B and $\theta_o = 94^\circ$ and 96° .

Fig. 19. Chromaticity diagram for Model C and $\theta_o = 90^\circ$ and 92° .

Fig. 20. Chromaticity diagram for Model C and $\theta_o = 96^\circ$.

Fig. 21. Chromaticity diagram for Model D and $\theta_o = 92^\circ$ and 96° .

Fig. 22. Chromaticity diagram for Model E and $\theta_o = 92^\circ$ and 96° .

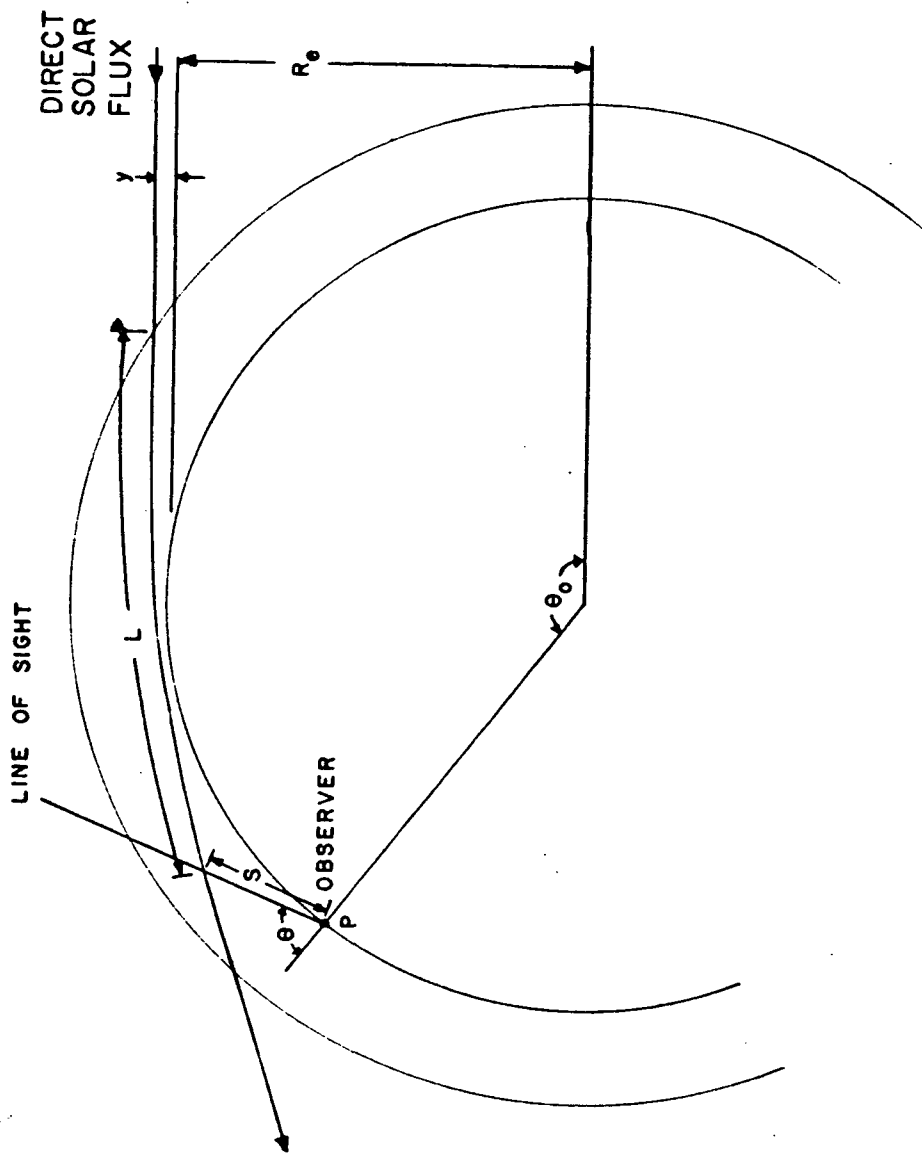


Fig. 1

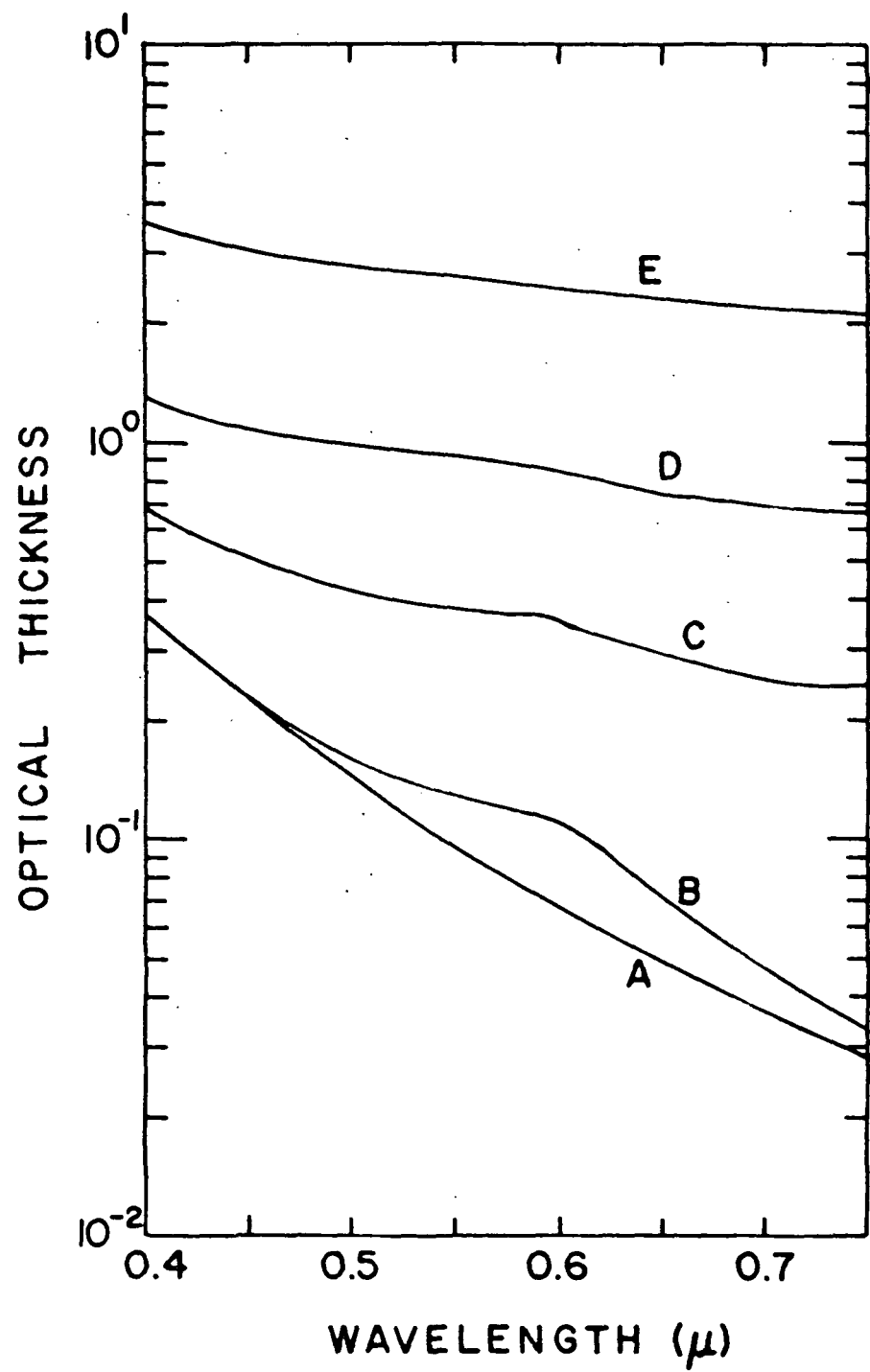


Fig. 2

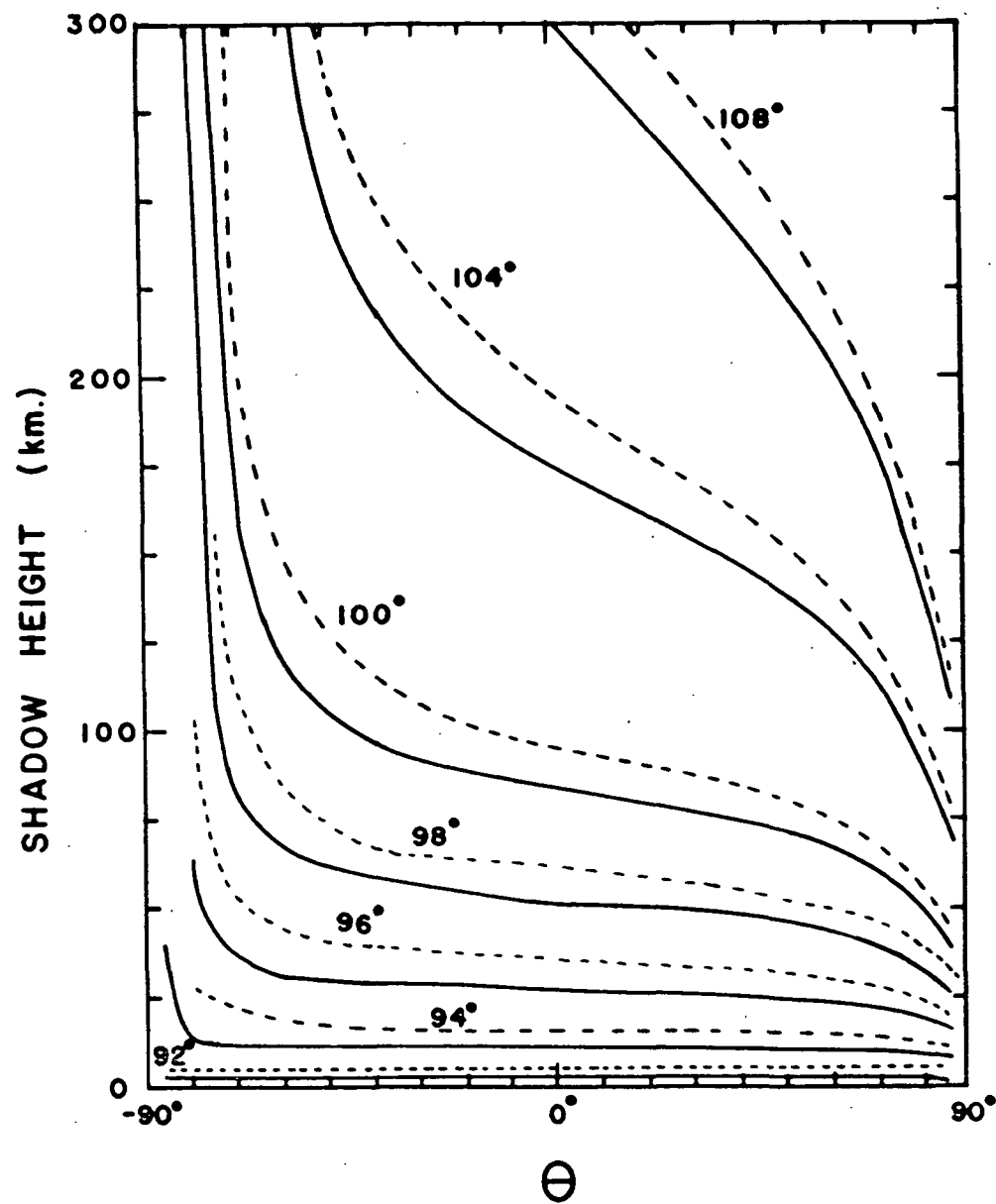


Fig. 3

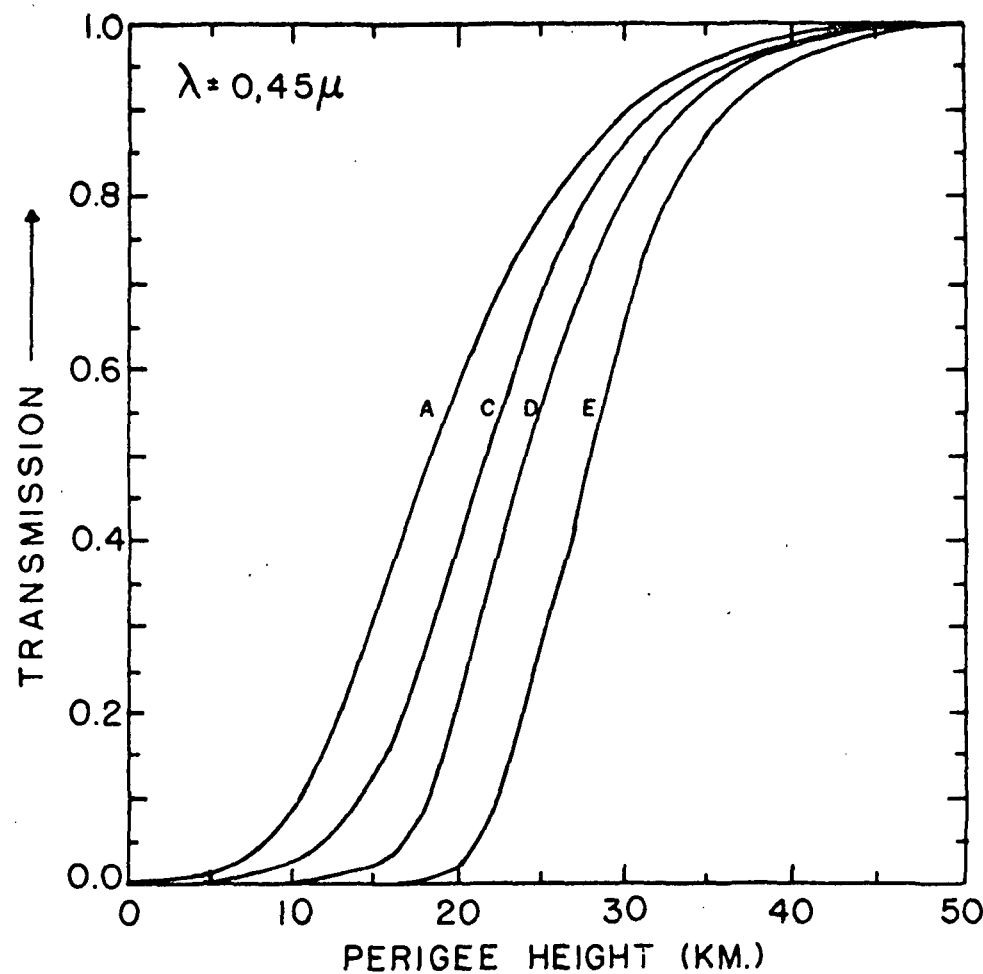


Fig. 4

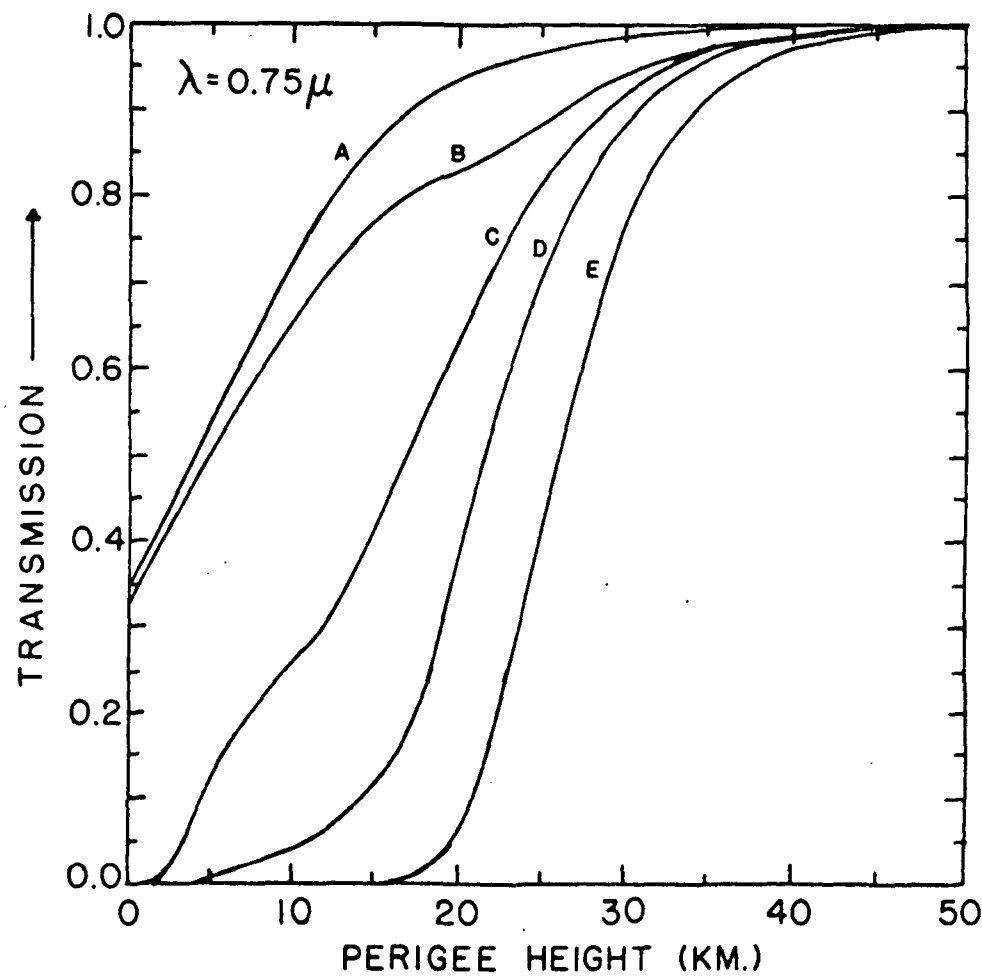


Fig. 5

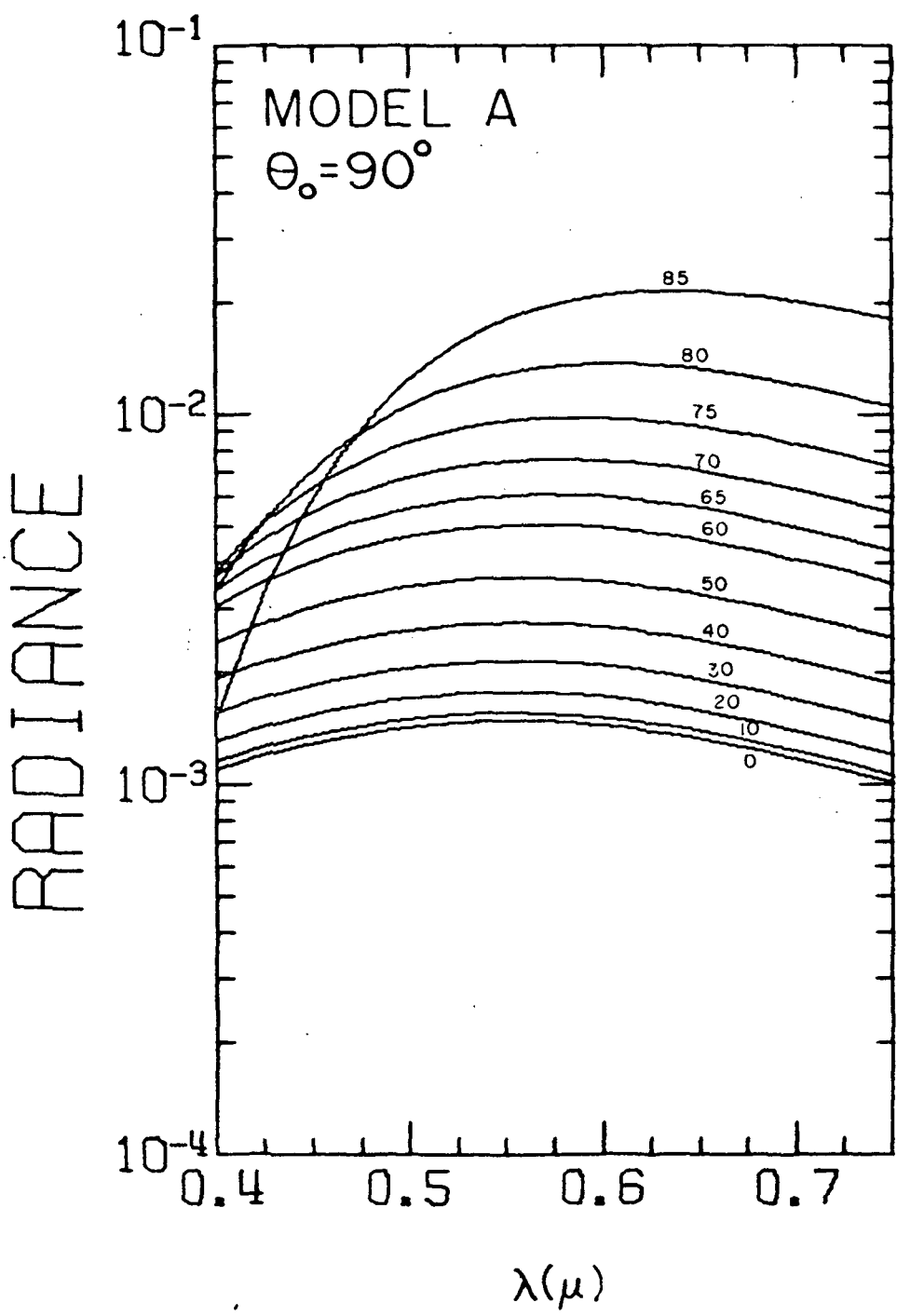


Fig. 6

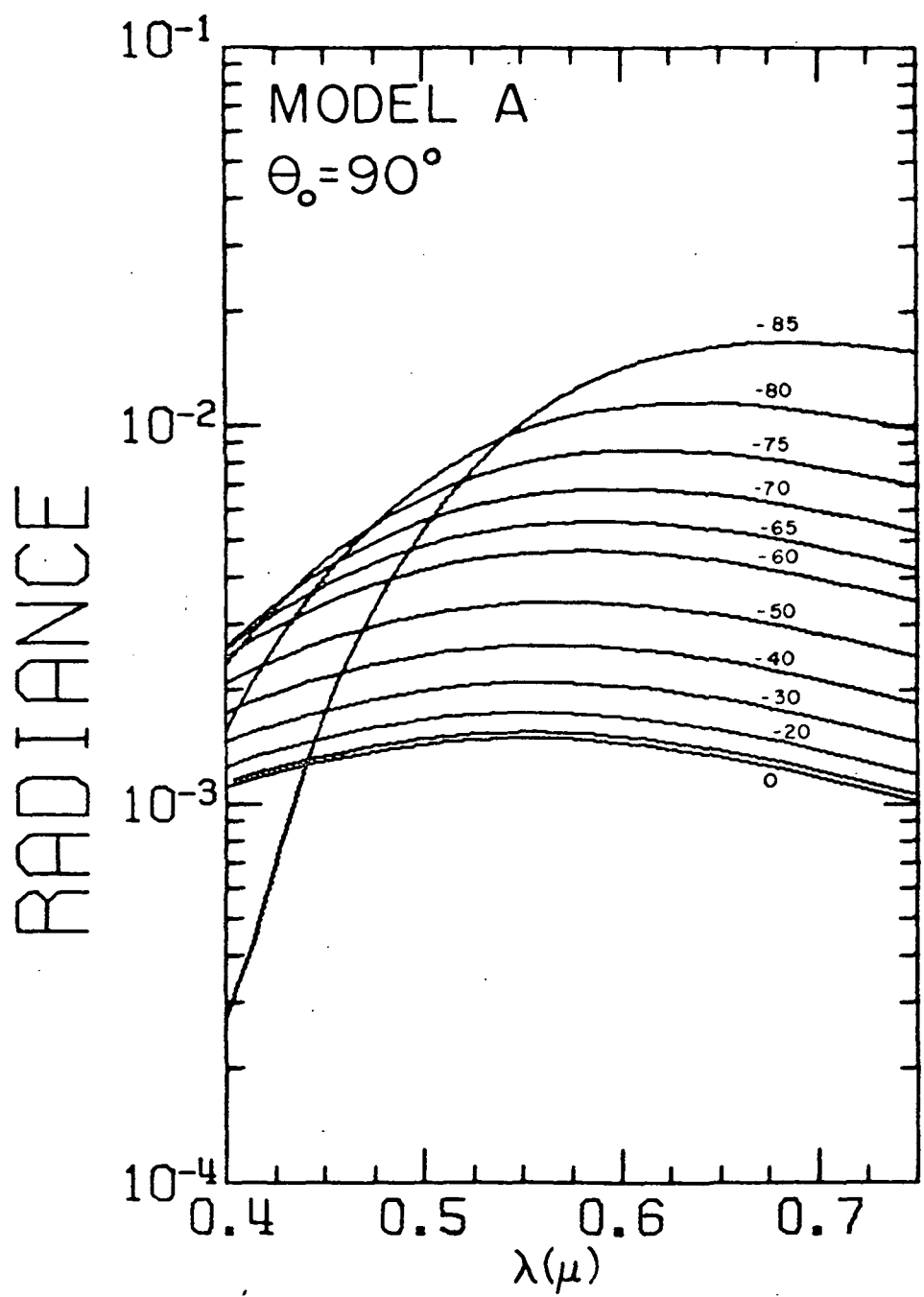


Fig. 7

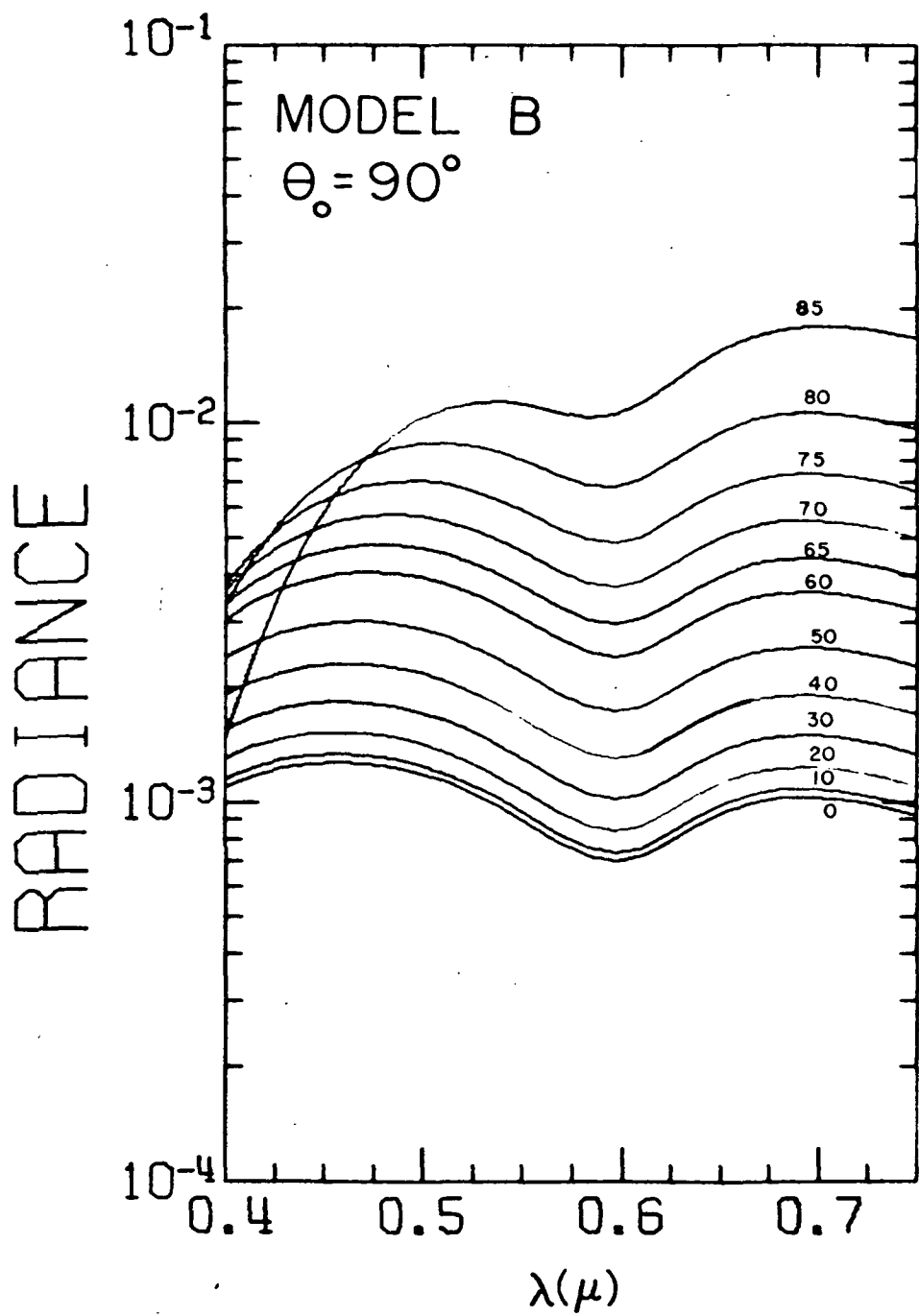


Fig. 8

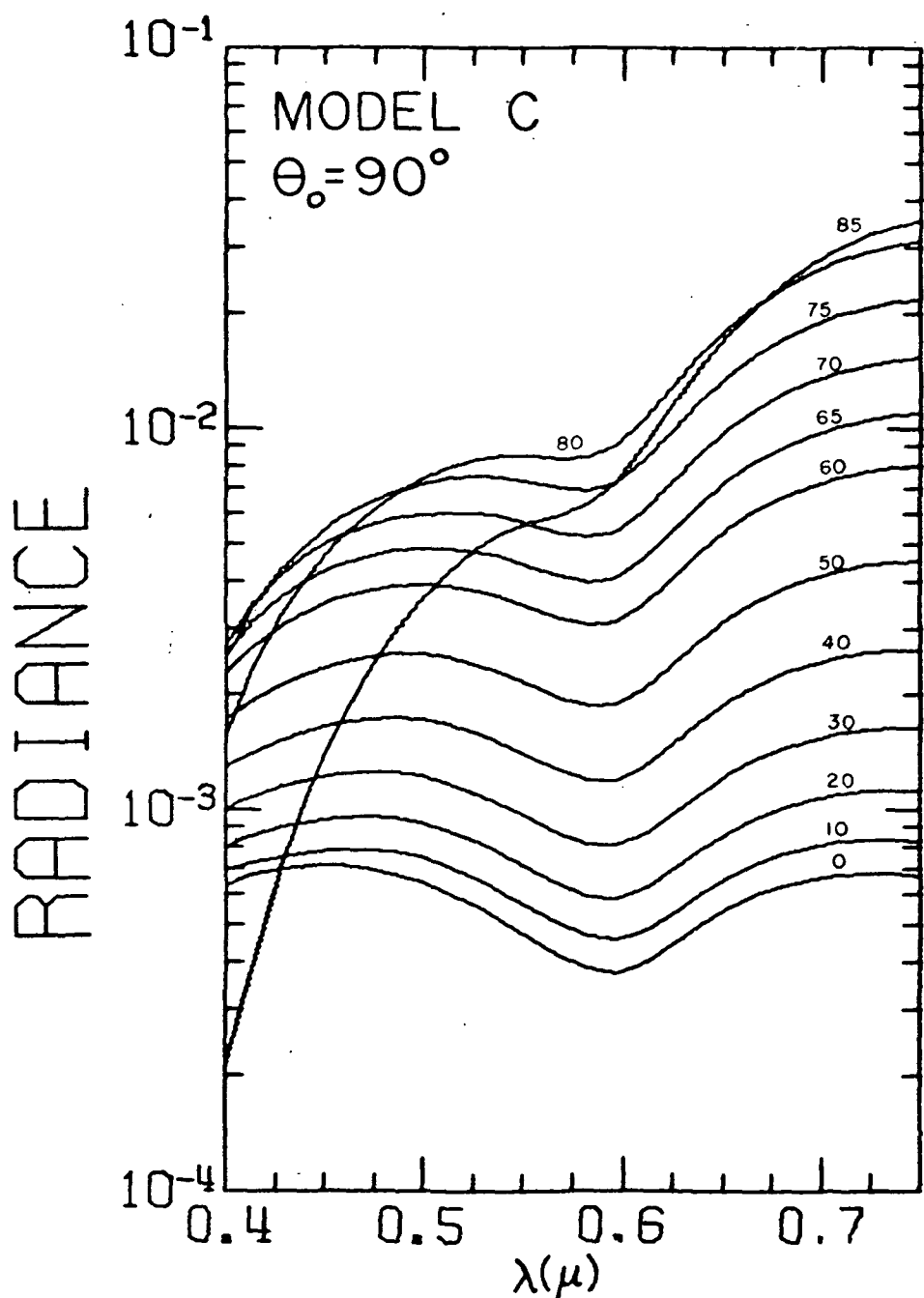


Fig. 9

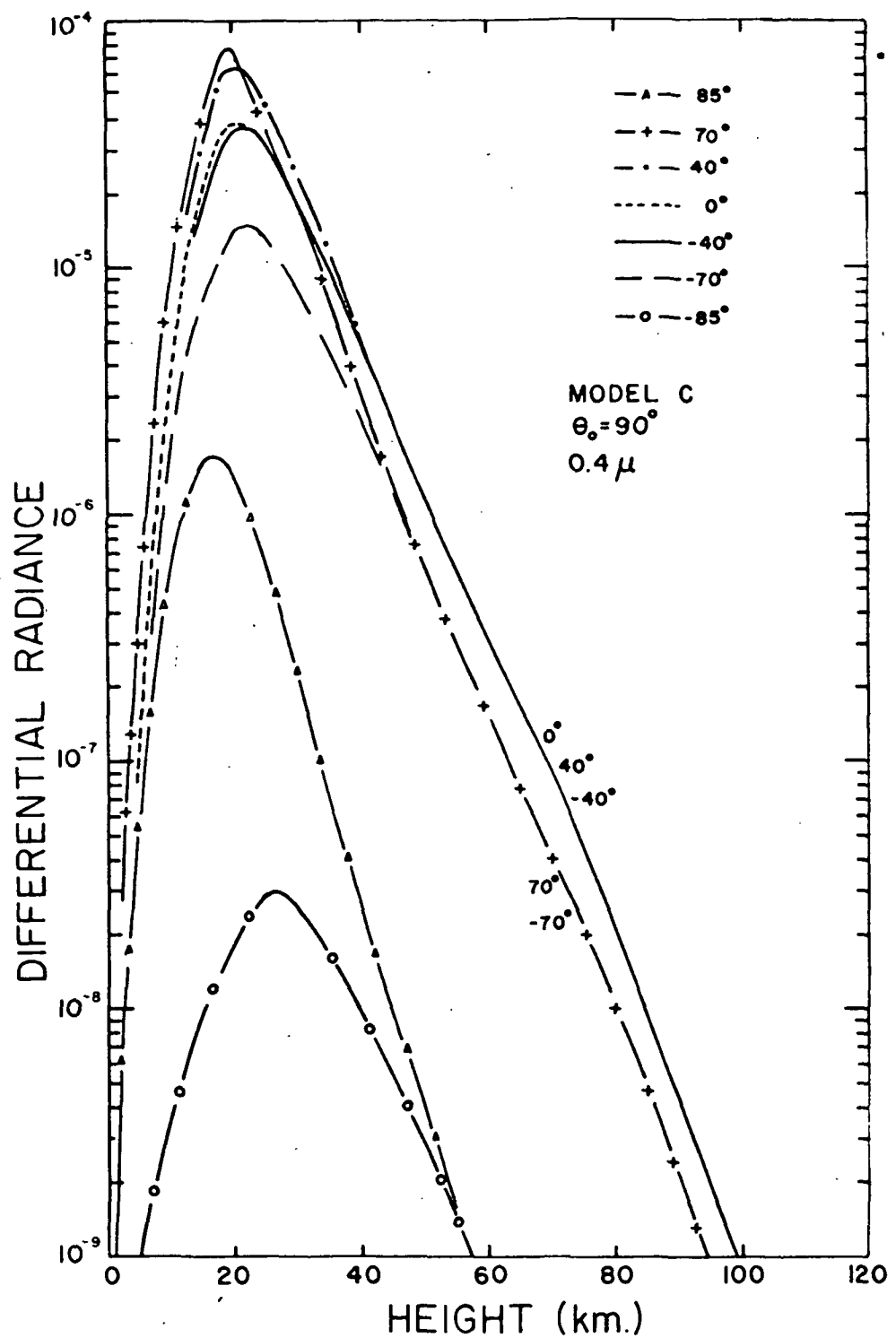


Fig. 10

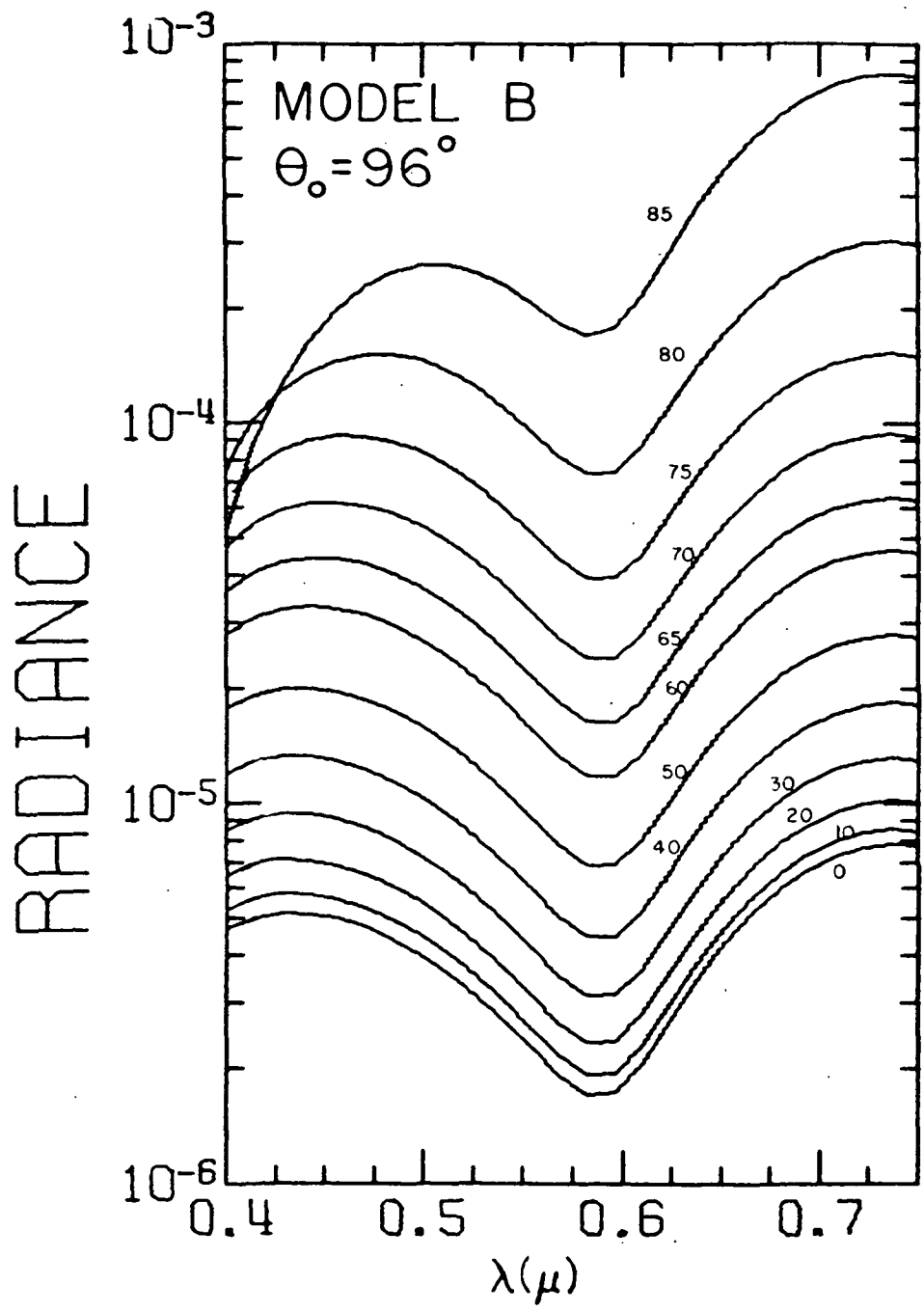


Fig. 11

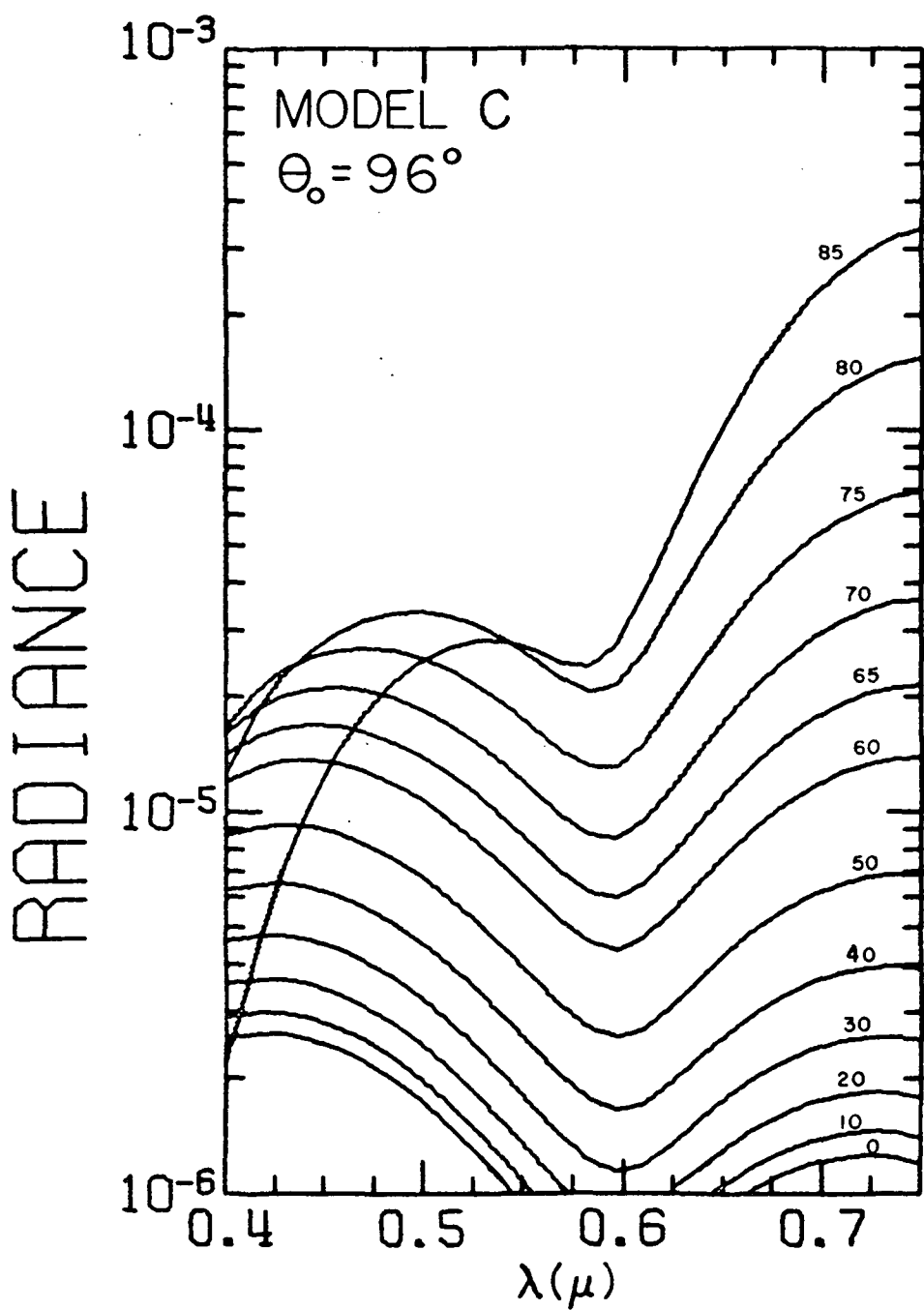


Fig. 12

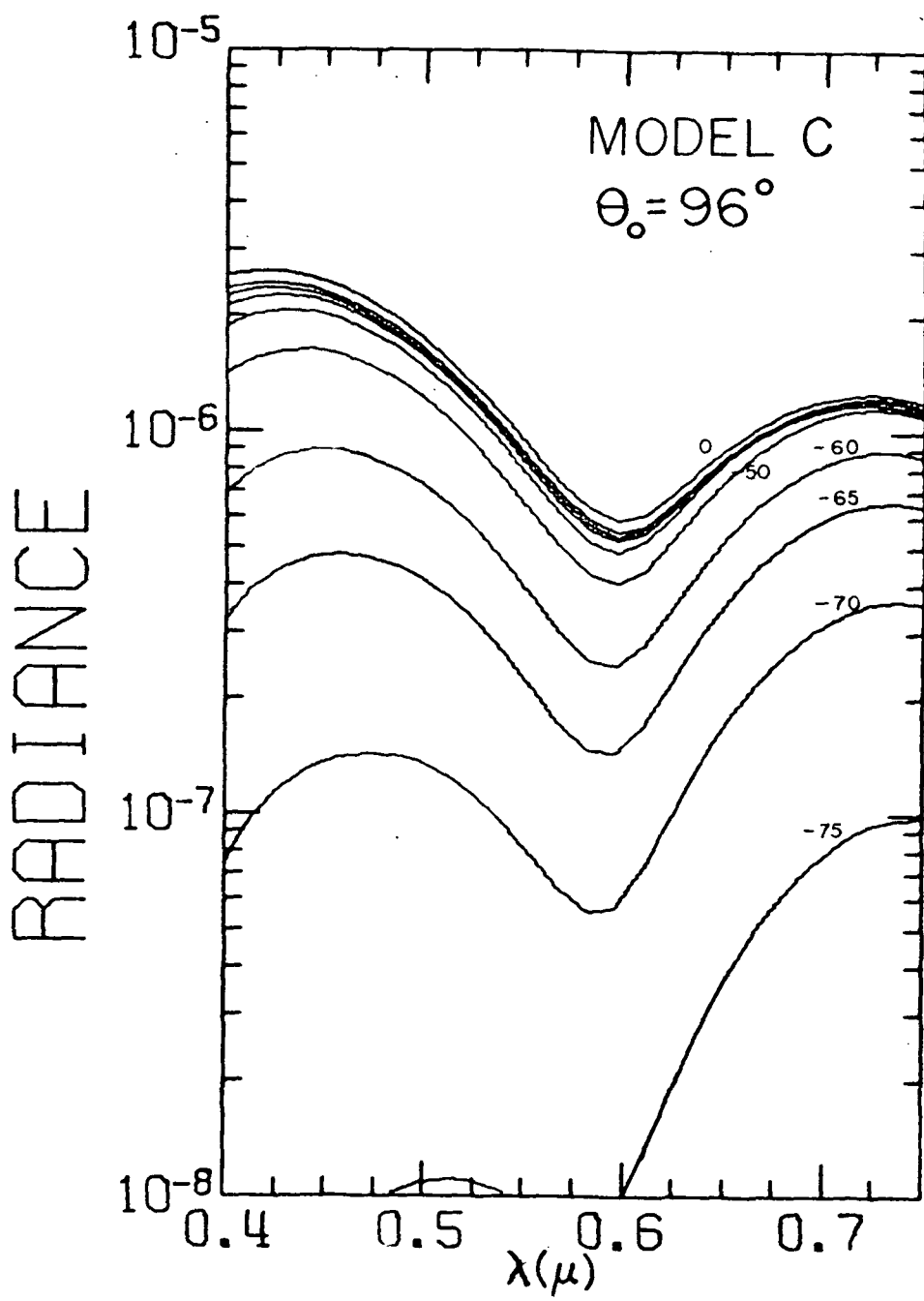


Fig. 13

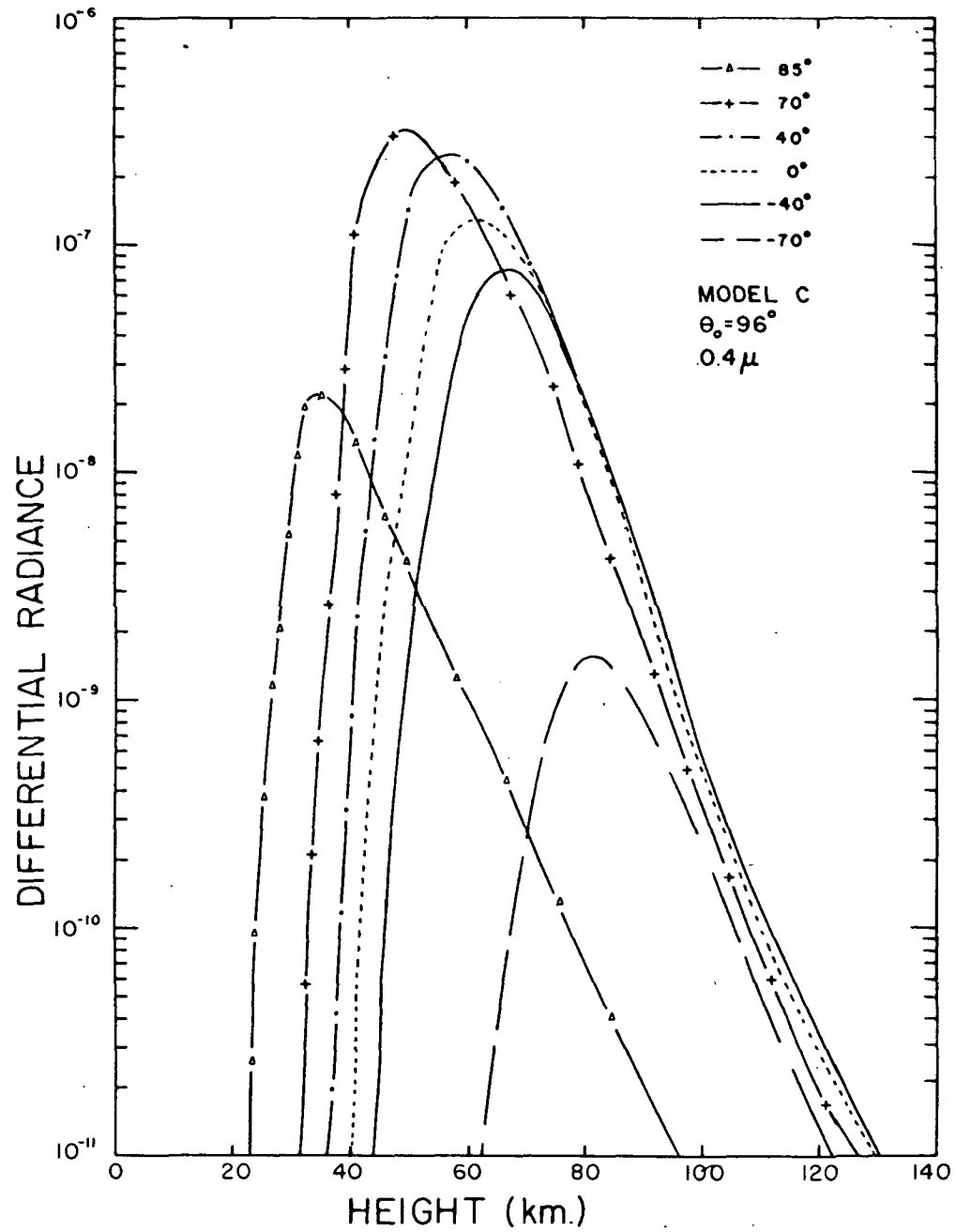


Fig. 14

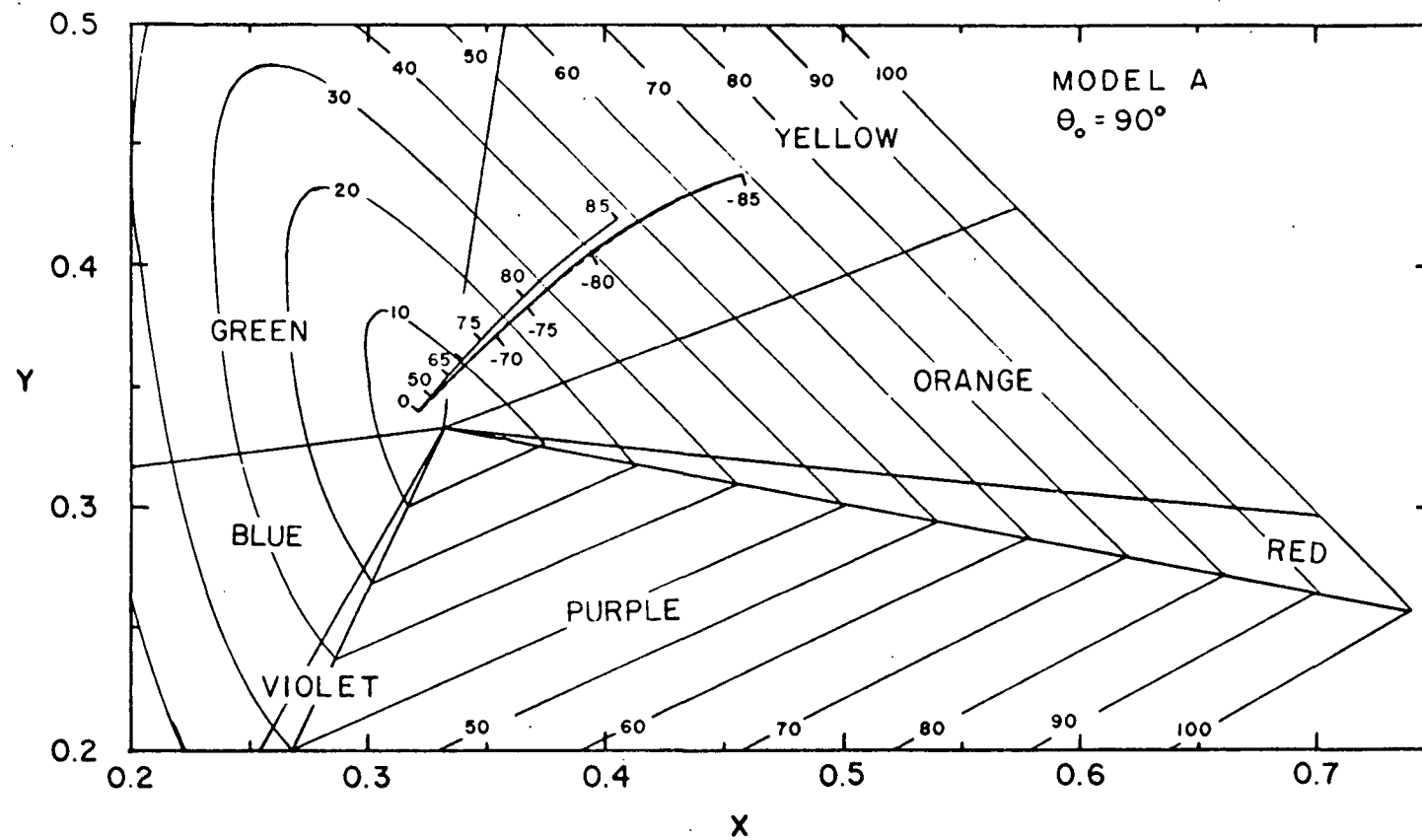


Fig. 15

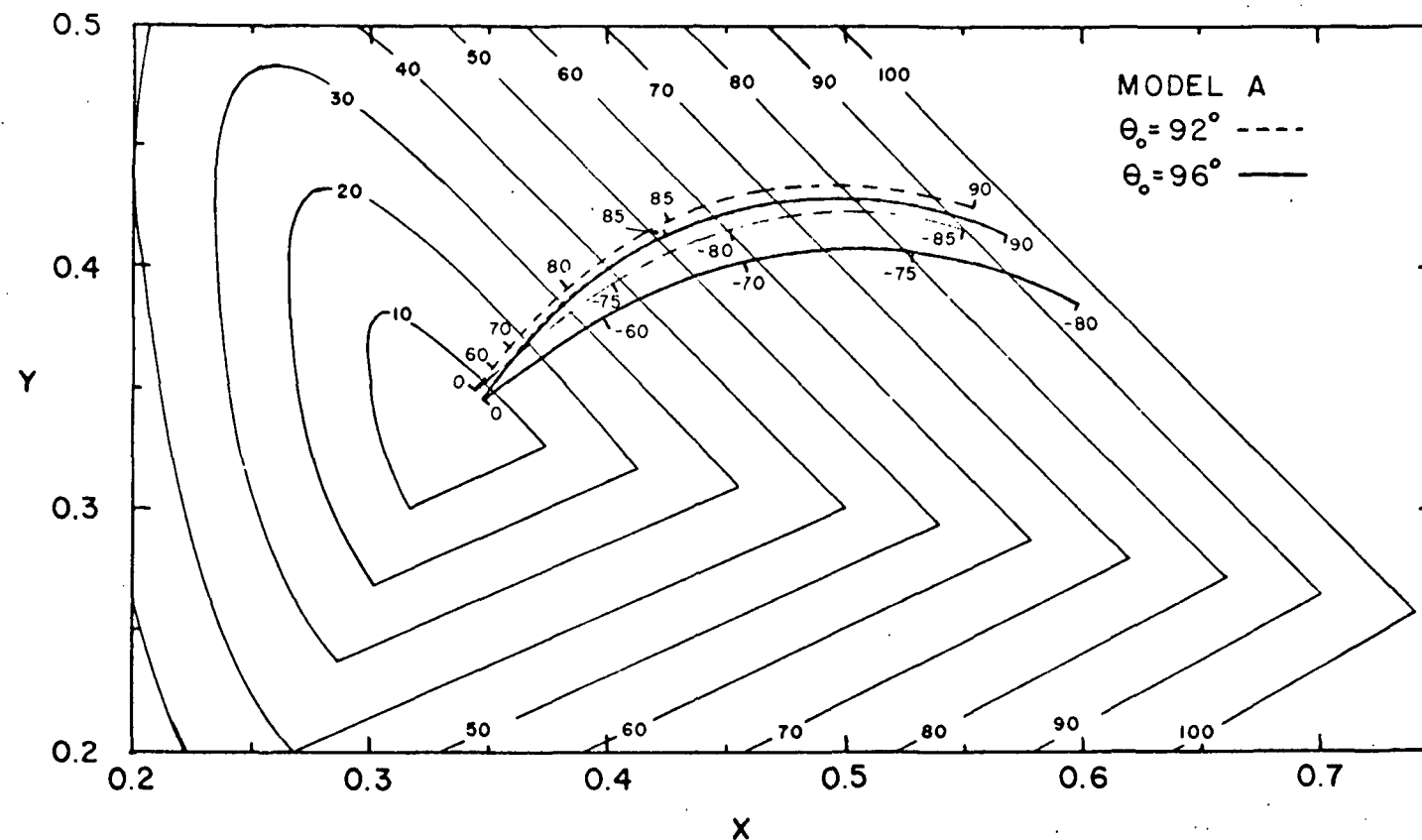


Fig. 16

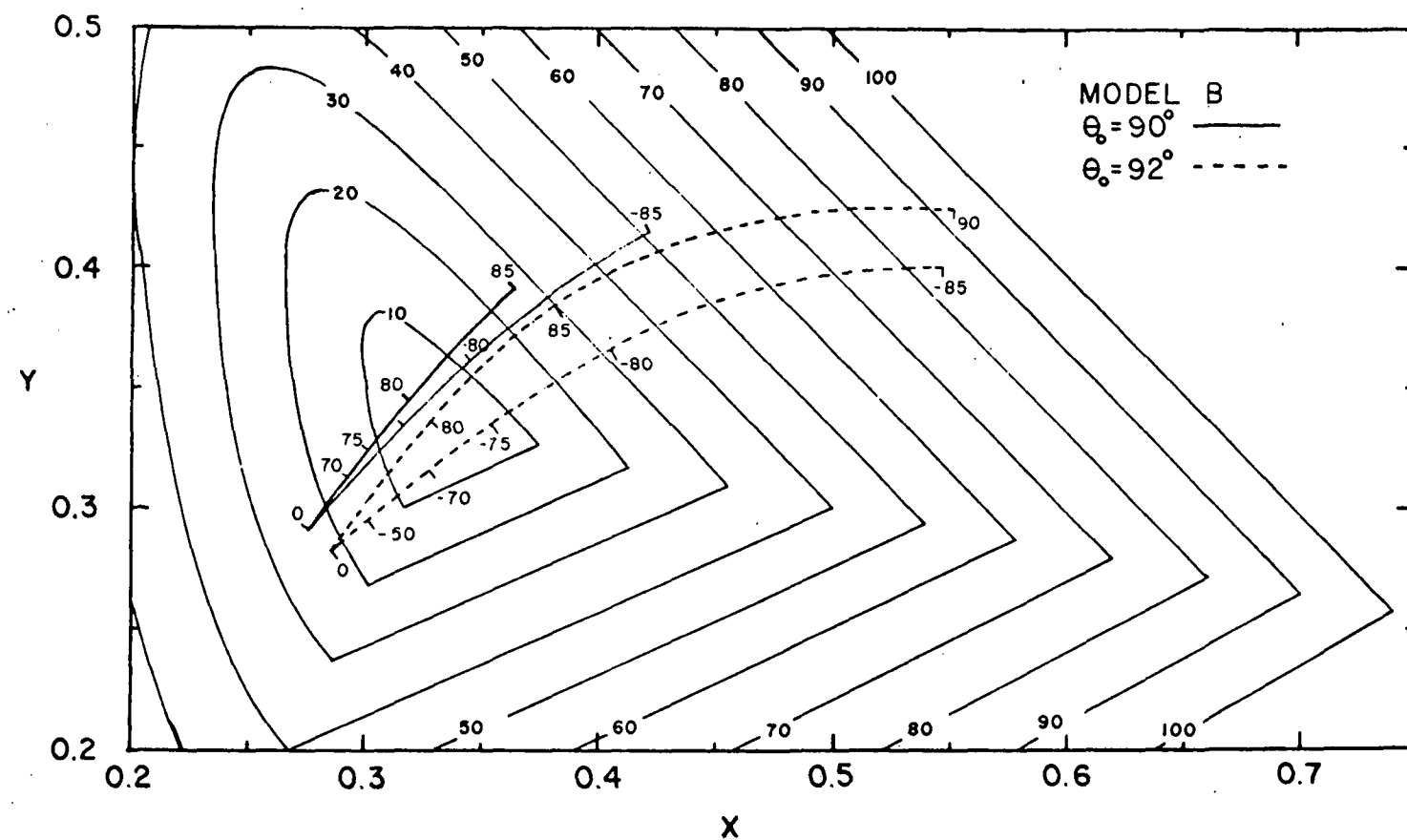


Fig. 17

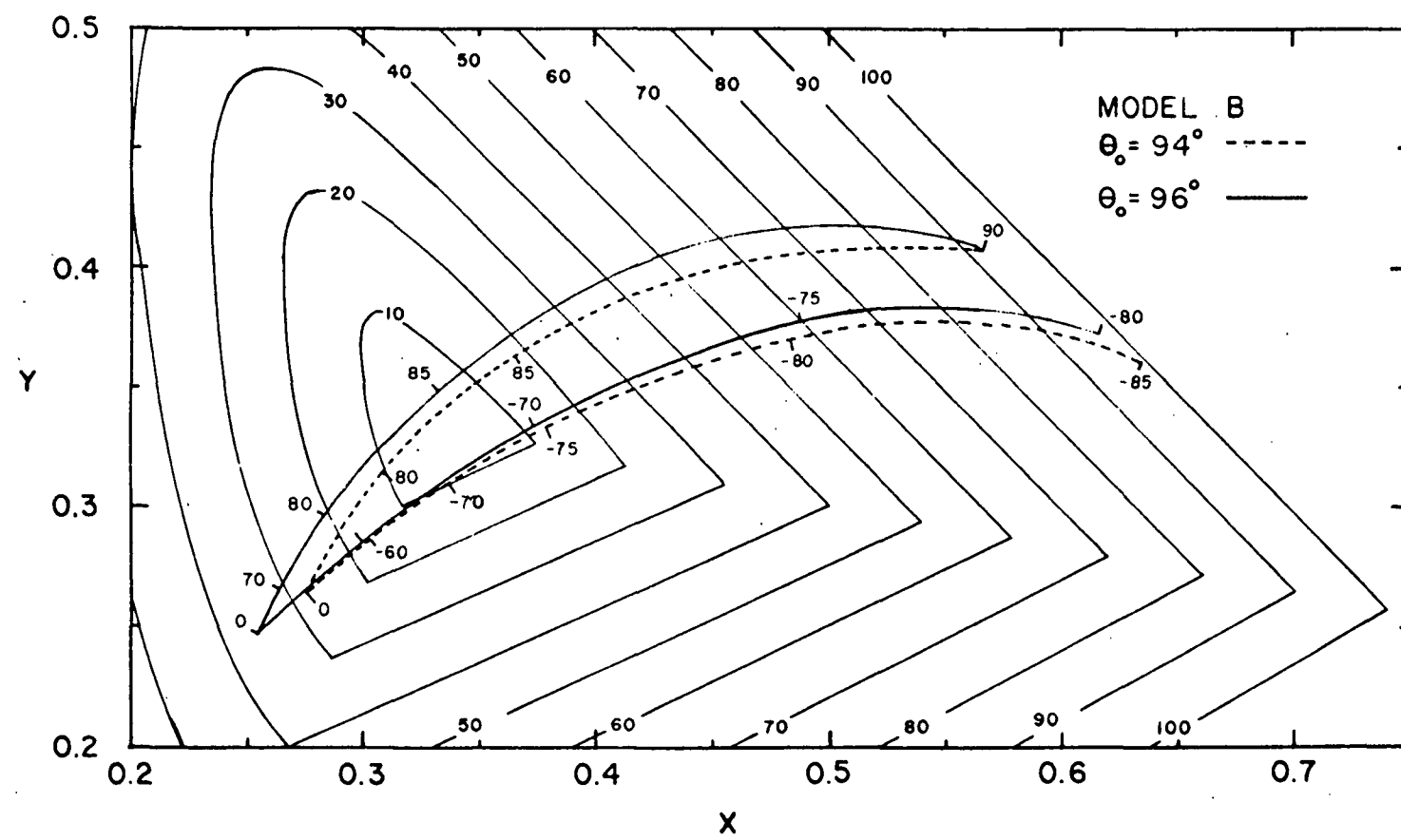


Fig. 18

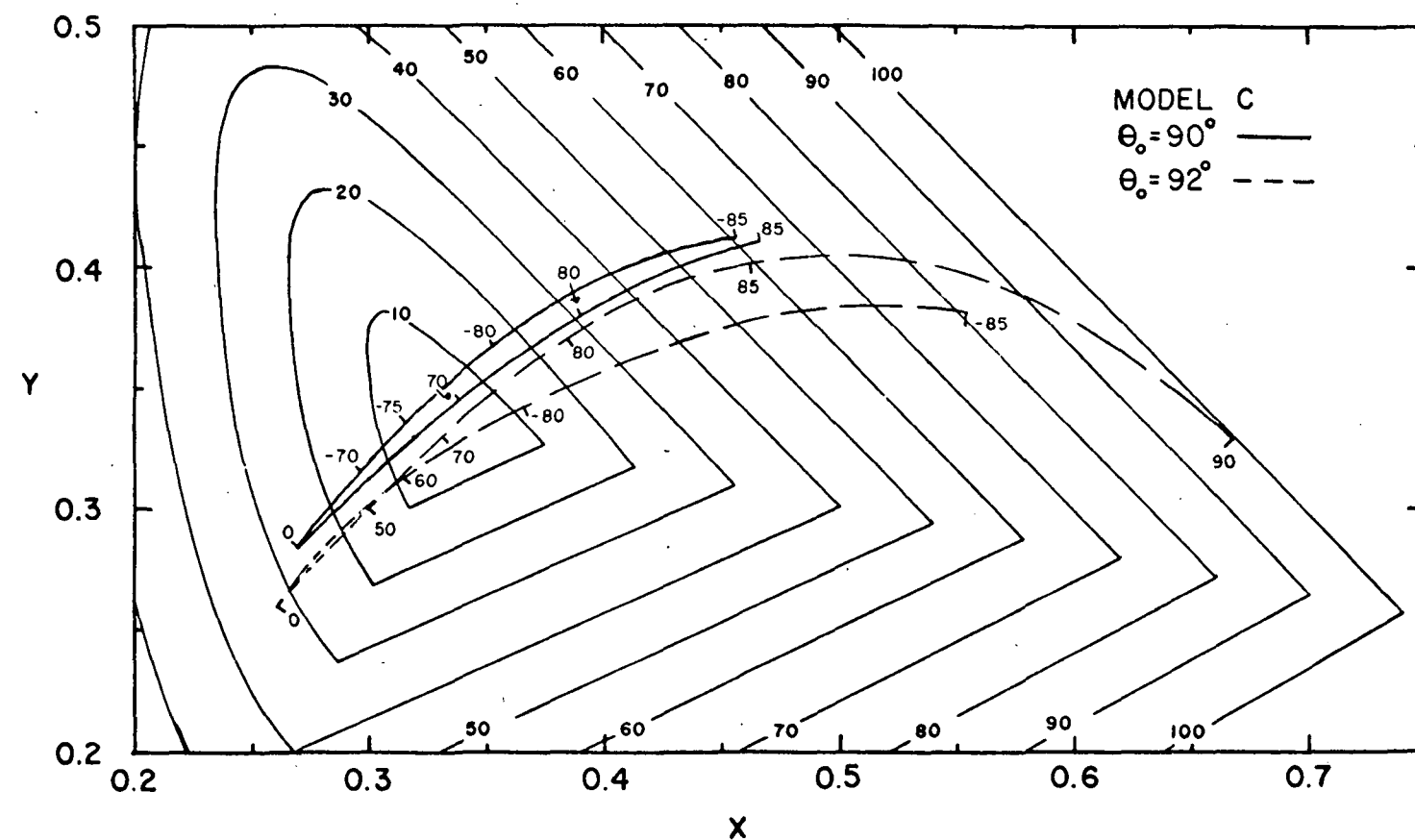


Fig. 19

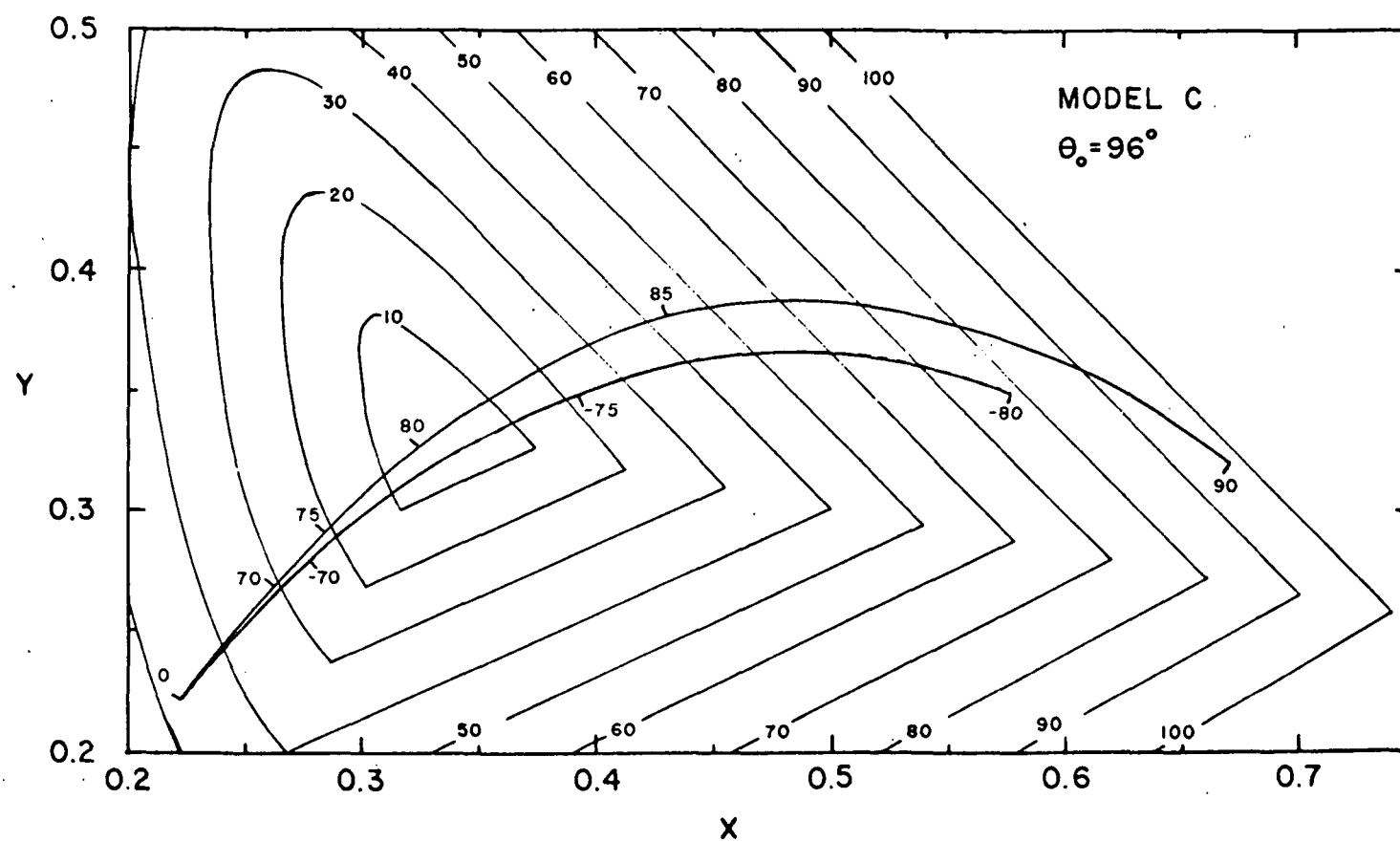


Fig. 20

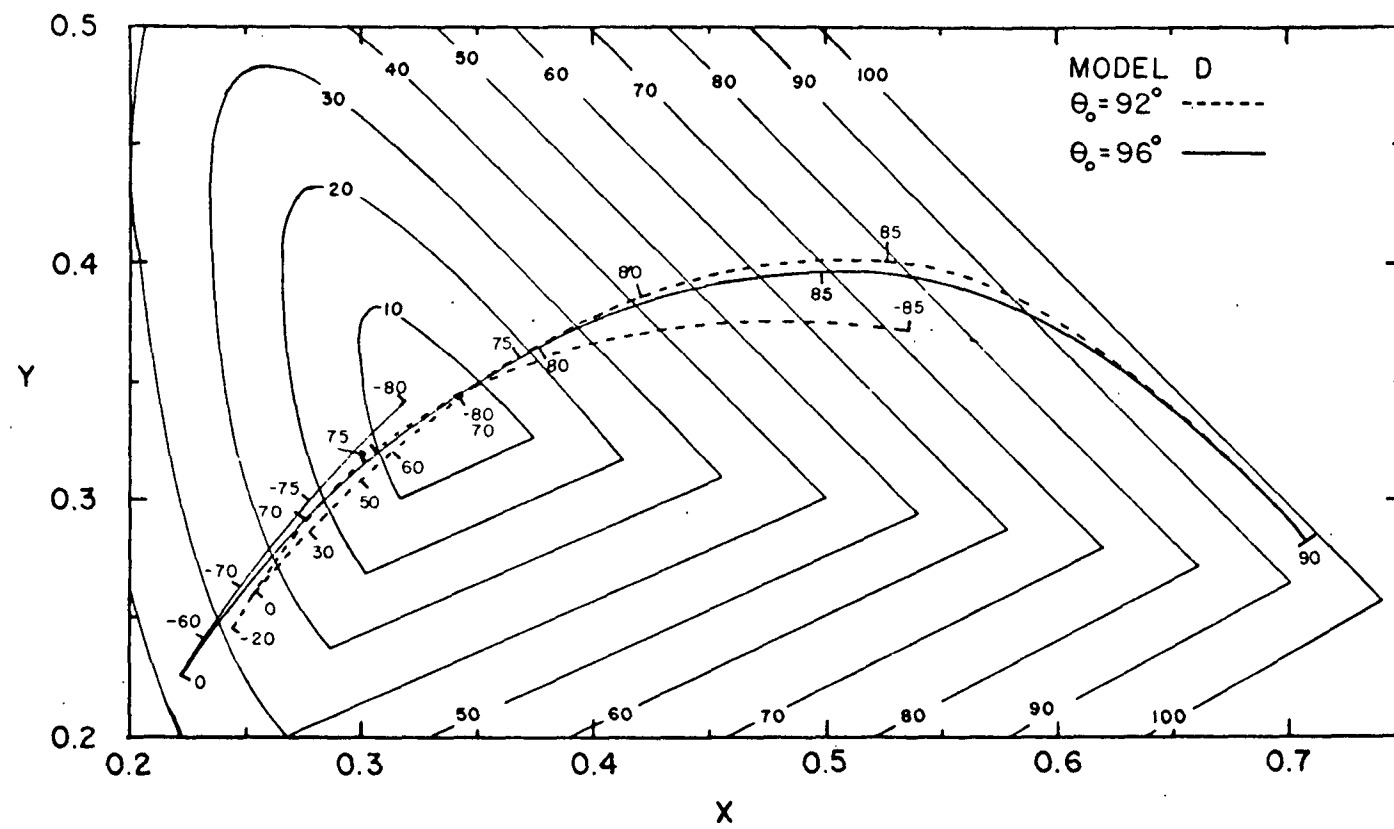


Fig. 21

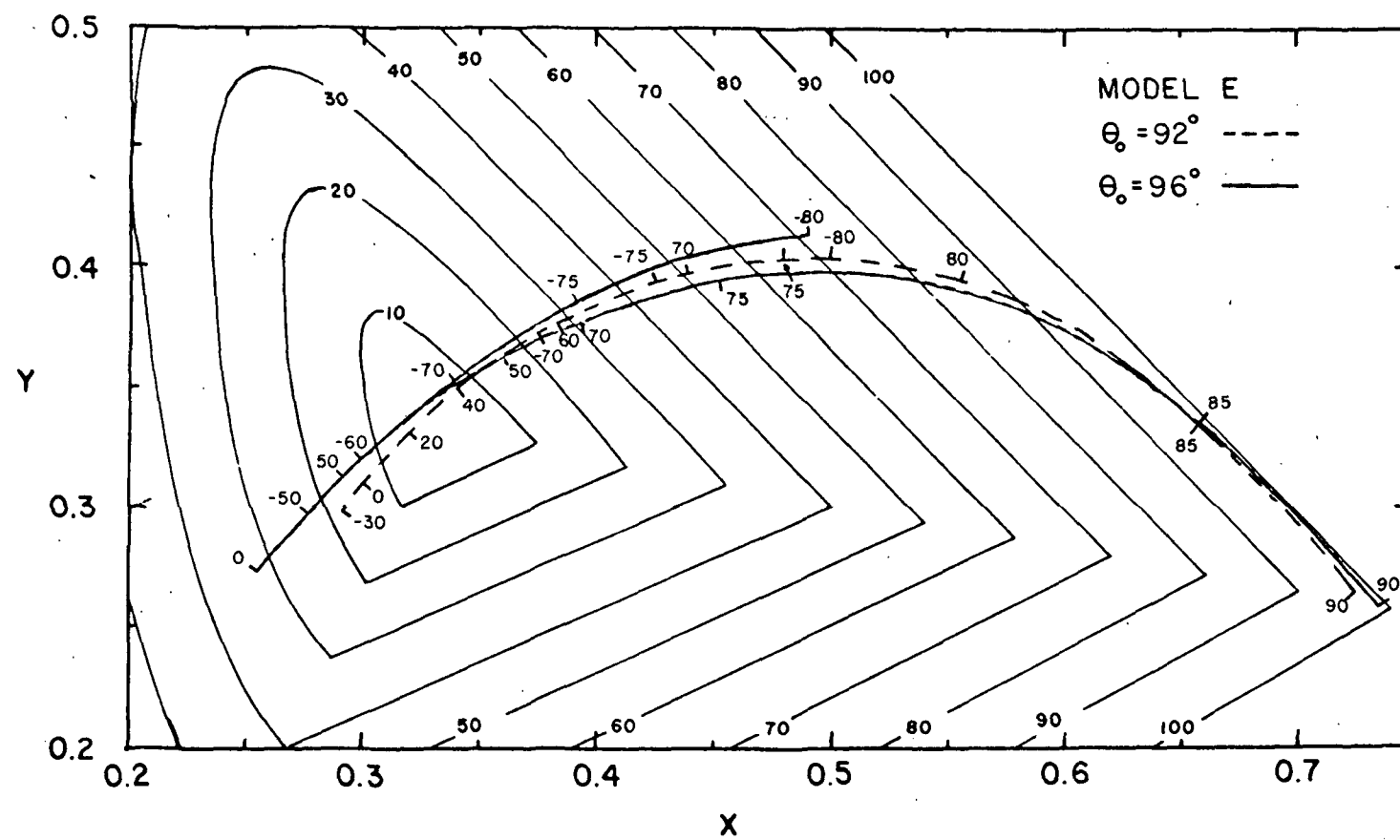


Fig. 22